Solid Earth

# Post-Hercynian ultrahigh-temperature tectono-metamorphic evolution of the Middle Atlas lower crust (central Morocco) revealed by metapelitic granulite xenoliths

**Abdelkader El Maz[1], Alain Vauchez[2], and Jean-Marie Dautria[2]**

[1]Department of Geology, University of Moulay Ismaïl, Meknes, Morocco
[2]Geosciences Montpellier, Montpellier University and CNRS, 34095 Montpellier, France

**Correspondence:** Abdelkader El Maz (elmazabdel@yahoo.fr)

**Abstract.** The study of metapelitic sillimanite- and garnet-bearing granulite xenoliths brought to the surface by the basanite of the 650 ka Tafraoute maar shed new light on the lower crust of the Tabular Middle Atlas (Morocco). Two main types of granulites are distinguished: (1) layered quartzo-feldspathic and (2) unlayered restitic. Mineralogy, petrology, $P$–$T$ estimates, and electron backscatter diffraction (EBSD) data support that these granulites underwent two successive tectono-metamorphic events before their entrapment in lava. During the first event, probably the Hercynian orogeny, the Tafraoute lower crust acquired its foliation and primary paragenesis, likely including kyanite; it yields $P$ and $T$ conditions of $1.1 \pm 0.1$ GPa and 850–880 °C. The second event corresponds to a reheating up to ultrahigh temperatures ($1050 \pm 50$ °C) under slightly lower-pressure conditions ($0.9 \pm 0.1$ GPa). This led first to the transformation of kyanite into large prismatic sillimanite. The latter displays uncommon evidence of the dislocation creep deformation of a moderate intensity that points to a tectonic episode occurring after their formation. After deformation has stopped, a reaction between sillimanite and garnet resulted in the crystallization of orthopyroxene and spinel-deformation-free coronas around garnets. Approaching the peak of temperature, anhydrous partial melting of quartzo-feldspathic layers likely occurred, and the resulting felsic melt spread into the rocks. This reheating event might be the consequence of the Late Permian to Mid Jurassic rifting that preceded the formation of the Middle Atlas range, possibly associated with underplating of hot gabbroic magma. This event was followed by gradual cooling down to ∼ 800 °C, leading to static crystallization of the felsic melt in the quartzo-feldspathic granulites. The last event susceptible to have affected the lower crust is the alkali magmatism active in the Middle Atlas during the Mio-Plio-Quaternary. In this context, the origin of restitic granulites is questionable. It may result either from the thermal event associated with the pre-alpine rifting or from the emplacement of basaltic dikes in the lower crust before the Quaternary eruption of the Tafraoute volcano. During this eruption, the studied granulites were entrapped in the ascending lava and very quickly transferred up to the surface, triggering the formation of small vesicular glass pockets. This study highlights the contrasted post-Hercynian evolution of the lower crust in the northern coastal alpine orogen (Rif) and the Tabular Middle Atlas; the first one underwent a tectonic exhumation without reheating during the Alpine orogeny, while the second one is characterized by a reheating to ultrahigh temperature, probably during the pre-alpine rifting, but was probably not or only slightly affected by the alpine events.

## 1 Introduction

The current knowledge of the lower crust of the Moroccan Mediterranean margin is based on a single occurrence of kyanite-bearing granulite outcropping in the Beni Bousera massif. This massif, located about 100 km SE of Tangier (Fig. 1), belongs to the Rif Coastal Alpine Range (north Morocco). The only window on the lower crust between the Mediterranean coast and the Anti-Atlas range (∼ 400 km
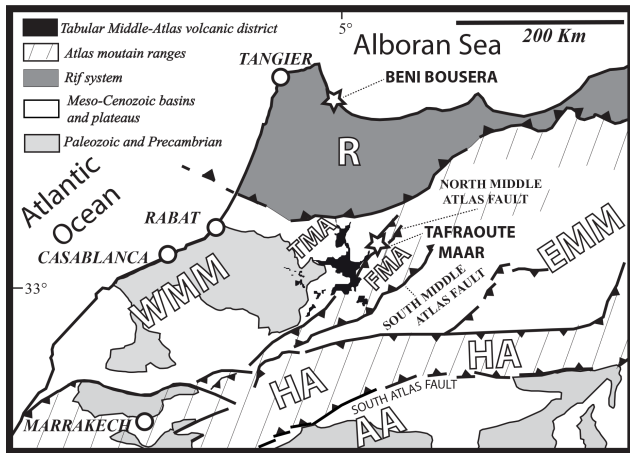
**Figure 1.** Schematic structural map showing the location of the Tafraoute maar and the Beni Bousera massif with regard to the main mountain ranges of Morocco (modified from Frizon de Lamotte et al., 2008, p. 135). AA, EMM, and WMM: Hercynian Anti-Atlas, eastern Moroccan Meseta, and western Moroccan Meseta, respectively. HA, FMA, TMA, and R: alpine ranges of the High Atlas, folded Middle Atlas, Tabular Middle Atlas, and Rif system, respectively.

south of the Rif) corresponds to granulite xenoliths sampled by the Plio-Quaternary alkali basalts of the Middle Atlas ($\sim$ 200 km south of the Rif; Fig. 1). One tuff ring of this magmatic district (Tafraoute maar; Fig. 1) is particularly rich in prismatic sillimanite-bearing granulite xenoliths. We have performed a new study of these granulites for two reasons: (1) their ultrahigh temperature (UHT) parageneses and (2) their major importance for the evolution of the deep crust of North Africa. Moukadiri and Bouloton (1998) have reported that these granulites might have been equilibrated at temperatures > 900 °C and, thus, that the lower crust likely underwent UHT conditions. However, these metamorphic conditions are still poorly constrained, and their relationships with deformation and geodynamic evolution of North Africa remain unknown.

Newton and Perkins (1982) and Bohlen (1991) have suggested that the estimated peak metamorphic conditions for granulitic formations cluster within a relatively narrow field of 0.65 to 0.9 GPa and 700 to 850 °C near the kyanite–sillimanite equilibrium boundary. Based on a large set of granulites from various locations around the world, Harley (1989) emphasized that more than 50 % of the granulites fall outside the $P–T$ field defined above, especially with temperatures higher than 900 °C. For instance, ultrahigh-temperature granulites (> 900 °C; 0.7–1.3 GPa) have been described in more than 50 localities around the world (e.g., Harley, 1998; Ouzegane et al., 2003a, b; Baldwin et al., 2005; Kelsey and Hand, 2015). UHT metamorphism is marked by (a) high $Al_2O_3$ contents (8 wt %–12 wt %; Harley, 1998) in orthopyroxene (Opx), coexisting with garnet (Grt) and silli-

manite (Sil) or sapphirine, and (2) the presence of mesoperthitic feldspar and high Zr contents in rutile (> 3500 ppm; Harley, 2008). Diagnostic mineral assemblages such as sapphirine + quartz (Qz), Opx + Sil + Qz, spinel (Sp) + Qz, corundum (Crn) + Qz and the presence of osumilite (Os) also support UHT conditions (e.g., Hensen and Green, 1973; Guiraud et al., 1996a–b; Harley, 1998, 2008; Kelsey and Hand, 2015). A pending question is how the lowermost continental crust may reach such high temperatures for such moderate pressures, considering that the temperature at the base of the crust is buffered around 850 °C by fluid-absent melting (Vielzeuf and Holloway, 1988; Vielzeuf et al., 1990). In refractory granulites, UHT metamorphism can easily develop if there is a significant heat supply, for instance due to emplacement of a large volume of mafic magma (Raith et al., 1997; Martignole and Martelat, 2003; Barbosa et al., 2006).

The study presented here combines petrography, mineral chemistry, thermobarometric estimates, and crystallographic-preferred orientation (CPO) measurements. The results of this study shed new light on the nature and evolution of the lower crust of this part of the Middle Atlas Alpine range since the Hercynian times.

## 2  Geological setting

In Morocco, Hercynian metamorphic rocks are exposed in the north (Rif) and in the center (Meseta). In the Meseta, the highest metamorphic ones consist of pelitic micaschists bearing Grt + staurolite + kyanite (Ky), corresponding to a medium-grade Barrovian-type metamorphism (Piqué and Michard, 1989; Hoepffner et al., 2005; Chopin et al., 2014). In the Rif, which is an alpine orogenic belt resulting from the Alboran terrane–Africa Miocene collision, slices (about 150 m thick) of lower-crustal granulites were exhumed simultaneously with the Beni Bousera peridotites massif (Kornprobst, 1969; El Maz and Guiraud, 2001; Álvarez-Valero et al., 2014). The primary paragenesis of Beni Bousera granulites (Grt + Ky + rutile (Rt) + biotite (Bt) + plagioclase (Plg) + K-feldspar (KF) + Qz + monazite + zircon) was dated at 284 ± 27 Ma (U–Th–Pb in monazite included in Grt; Montel et al., 2000), 286–264 Ma, and 300–290 Ma (zircon U–Pb dating; Melchiorre et al., 2017; Rossetti et al., 2020). The $P$ and $T$ equilibrium conditions of this paragenesis were estimated at 1.2 GPa and 850 °C (El Maz and Guiraud, 2001; Álvarez-Valero et al., 2014; Rossetti et al., 2020).

A total of 200 km south of the Rif, the Middle Atlas range (MA; Fig. 1) is almost entirely made of Liassic-to-Mid-Jurassic dolomitic limestones lying on a thick Triassic clay-evaporite series locally associated with doleritic basaltic flows, as in central Morocco (Fiechtner et al., 1992). The MA, like the High Atlas range further south, was formed during the alpine orogeny through the inversion of a pre-existing Triassic-to-Jurassic rift system linked to the central

Atlantic Ocean opening (e.g., Mattauer et al., 1977; Frizon de Lamotte et al., 2000; Michard et al., 2008, and references therein). A NE–SW-trending major transcurrent fault (north Middle Atlas Fault) separates the MA in two domains, a folded one and a tabular one, respectively, located SE and NW of the fault (Fig. 1). During the Cenozoic, the MA underwent an uplift probably related to a mantle upwelling and a lithospheric thinning (e.g., El Messbahi et al., 2015, and references therein). Mio-Plio-Quaternary alkali basaltic activity coeval with this upwelling occurred in this region (El Azzouzi et al., 2010). The most recent volcanic edifices (23 strombolian cones and 30 hydrovolcanic edifices; El Messbahi et al., 2020) are clustered within an area of $\sim 500\,\mathrm{km}^2$ located in the core of the tabular domain (Fig. 1). Many of them contain xenoliths of the lithospheric mantle (e.g., El Messbahi et al., 2015, and references therein) and some contain xenoliths of a lower crust (Moukadiri and Bouloton, 1998). The Tafraoute maar ($33°31'29''\,\mathrm{N}$–$4°41'35''\,\mathrm{W}$; $550\,\mathrm{ka}$; El Messbahi et al., 2020), where the granulitic xenoliths of metapelitic origin studied here have been collected, is located northeastward of the main volcanic area (Fig. 1). This volcanic edifice corresponds to a semi-circular tuff ring about $2\,\mathrm{km}$ long and $500\,\mathrm{m}$ wide, deposited around a shallow explosion crater (El Messbahi et al., 2020). The Tafraoute tuffs contain a large variety of xenoliths, in addition to metapelitic granulites, namely (i) partially recrystallized garnet-rich metadiorites free of aluminosilicate, with some of them containing minor biotite; (ii) undeformed to weakly deformed alkali to transitional gabbros similar to those found in the central High Atlas and dated to the Mesozoic (Haillwood and Mitchell, 1971; Smith and Pozzobon, 1979); and (iii) ultramafic rocks (kaersutite, websterite, diopsidite, and spinel peridotite; El Messbahi et al., 2015). Euhedral kaersutite megacrysts (up to $10\,\mathrm{cm}$ long), a phase typically associated with basanitic magmatism, are abundant. In addition, dark blue corundum euhedral crystals (up to $2\,\mathrm{cm}$ large) are frequent. Such crystals are usually considered to result from the mixing of felsic melt with a Si-poor magma (Guo et al., 1996; Sutherland et al., 1998; Giuliani et al., 2009).

In this work, the petrological characteristics of the granulites from the Tafraoute maar will be compared with those from the Beni Bousera massif. Determining similarities and differences in the granulites from these two sites would allow comparing the tectono-metamorphic evolution of the lower crust of the Tabular MA with the better-known Rif one.

## 3 Sampling and analytical methods

Tens of metapelitic granulite xenoliths, between 10 and 75 cm in size, have been collected in the Tafraoute tuffs (Fig. 2). They can be macroscopically divided in two groups on the basis of mineralogy and structure, i.e., quartzo-feldspathic granulites (QFGs) with a well-marked layering
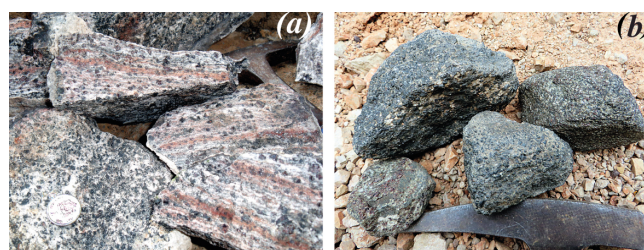
**Figure 2.** Pictures of quartzo-feldspathic **(a)** and restitic **(b)** granulite samples collected in the Tafraoute tuffs. The coin diameter in panel **(a)** is 2 cm.

(Fig. 2a) and restitic ones (RGs) almost unlayered and free of quartz and feldspars (Fig. 2b). Thin sections have been prepared for a selection of samples and studied under an optical microscope. From this study, five metapelitic xenoliths representative of the lower crust of Tafraoute have been selected for electron backscatter diffraction (EBSD) and microprobe analysis, with three QFGs (G2, 50 cm in size; G3, 75 cm; G4, 10 cm) and two RGs (TAF500 and TAF501; $\sim 10\,\mathrm{cm}$).

Major elements composition of rock-forming minerals was analyzed at Microsonde Sud facility (University of Montpellier, France) using a Cameca SX 100 electron microprobe equipped with five wavelength-dispersive spectrometers. Operating conditions comprised an acceleration voltage of $20\,\mathrm{kV}$ and a $10\,\mathrm{nA}$ beam current. The counting time was 15 min for Zr in rutile and Ti in zircon and 3 min for major elements.

Crystallographic mapping and crystallographic-preferred orientation measurements were performed on the five selected samples using indexing of EBSD patterns obtained in a Camscan Crystal Probe X500FE scanning electron microscope (Geosciences Montpellier, University of Montpellier, France) equipped with EBSD and energy dispersive spectroscopy (EDS) detectors, both controlled by the AZtecHKL acquisition software (Oxford Instruments). Diffraction pattern acquisition was produced with an acceleration voltage of 17 to 21 kV and a working distance of $\sim 25\,\mathrm{mm}$. For each sample, EBSD data covering most of the thin section were acquired with a regular grid step between 12 and $16\,\mu\mathrm{m}$, depending on the grain size. In addition, a few more detailed maps of smaller areas have been acquired (step size between 3.5 and $5.5\,\mu\mathrm{m}$) to better characterize the relationships between phases in destabilization coronas around garnets. The raw indexation rate varies from 74 % to 80 %. Post-acquisition data processing was performed following the procedure described in detail in Baptiste et al. (2015), using Channel 5 software (Oxford Instruments) and the MTEX toolbox in MATLAB (http://mtex-toolbox.github.io/, last access: 24 October 2023; Hielscher and Schaeben, 2008; Bachmann et al., 2010, 2011; Mainprice et al., 2014), allowing the improvement of the indexation rate. EBSD maps were systematically checked against microscope observa-

tions to avoid over-extrapolation. Pole figures have been generated and rotated using MTEX. The orientation distribution functions (ODFs) were calculated using the de la Vallée Poussin kernel function with a half-width of 10°. Pole figures have been plotted using the mean orientation for each grain instead of the whole-pixel measurements to avoid over-representation of large crystals in the CPO.

# 4 Structure, modal composition, and mineral chemistry

Two thin section pictures of each granulite type (one under polarized light and the other under polarized–analyzed light) are shown in Fig. S1a–b in the Supplement. However, EBSD maps better reveal the composition and microstructure. Therefore, EBSD mapping has been performed for the five selected granulites (Figs. 3 and S3 to S7).

All studied samples contain prismatic sillimanite (Fig. 4), garnet, orthopyroxene, spinel, rutile, ilmenite, graphite, and zircon. Garnet is variably destabilized and surrounded by a kelyphitic corona, as illustrated by Figs. 5 and S2. Quartz and feldspars are abundant in the QFGs but scarce or lacking in the RGs. In addition, osumilite and corundum are present but rare: the first one was observed in both QFG and RG samples, while the second one was only found in some RGs. Brown glass is abundant in the RG samples and has only a minor amount in the QFGs.

Modal proportions of minerals (Table 1) have been evaluated from EBSD measurements. All studied samples display a foliation marked by the shape-preferred orientation of large sillimanite crystals. In the QFG, this foliation is also underlined by sometimes almost monomineralic layers of Qz, Plg, and KF.

## 4.1 The layered quartzo-feldspathic granulites (QFGs)

The QFGs display a large variety of modal compositions (Table 1) and microstructures (Fig. 3) essentially due to the degree of Grt breakdown and the habitus of feldspars and Qz. On the other hand, Sil displays similar characteristic in all samples. In addition, the major constitutive minerals display minor chemical variations (Tables S1 to S10). Sillimanite (18 vol %–25 vol %, depending on the sample) appears as large prismatic crystals ($\geq 1$ mm wide and up to 3 mm long) displaying evidence of dislocation creep intracrystalline deformation (Fig. 4a), with shape-preferred orientation, undulose extinction, and spaced subgrain boundaries perpendicular to cleavages and to the long axes of crystals (Fig. 4a). Some crystals are bent and exhibit fan-like subgrain boundaries (Fig. 4b), and clusters of minute sillimanite new grains ($\sim 10$–20 μm) occur within or at the rim of some large crystals (Fig. 4c). In several samples (e.g., G2; Figs. 3 and S3), Sil crystals often display serrated boundaries underlined by a thin discontinuous strip of interpenetrating tiny anhedral

crystals of spinel ($\leq 40$ μm) and quartz ($\leq 10$ μm). Some prismatic Sil display two cleavages at an angle of $\sim 74°$, similar to kyanite, suggesting that they represent a polymorphic species intermediate between these two aluminosilicates, as described by Leyreloup (1974), Lal et al. (1984), Raith et al. (1997), and Tong and Wilson (2006). The chemical composition of sillimanite (Table S1) is almost identical in all analyzed samples; the only noticeable peculiarity is their high Fe content ($0.9 < \%\, Fe_2O_3 < 1.4$).

Garnet (0.5 vol %–19 vol %) has a slightly variable composition from one sample to the other (Table S2). According to Yardley (1977), high-temperature garnets have flat compositional profiles; therefore, we only performed core and rim analyses, and no significant zoning was observed. Garnet is almost exclusively almandine (Alm)–pyrope (Prp) solid solution ($X_{alm} = 0.55$–0.62, $X_{prp} = 0.3$–0.42, $X_{Fe2+} = 0.55$–0.67), with relatively constant minor contents of grossular (Grs) ($X_{grs} = 0.05$–0.07) and spessartine (Sps) ($X_{sps} = 0.01$–0.03). These compositions fall in the field of Beni Bousera Grt ($X_{alm} = 0.5$–0.8, $X_{prp} = 0.1$–0.3, $X_{grs} = 0.03$–0.25, $X_{sps} = 0$–0.06, and $X_{Fe2+} = 0.6$–0.8; El Maz and Guiraud, 2001). Some crystals of garnet (e.g., in G3 Figs. 3 and S4) contain inclusions of Rt, ilmenite (Il), graphite (Gph), Plg, KF, and Qz. Garnet crystals have shapes varying from one sample to the other, depending on fracturing and breakdown. Garnet breakdown resulted in the formation of reactional coronas whose width is variable, depending on samples (Figs. 3 and 5a). For instance, the replacement of garnet is minimal in sample G3 and maximal in G2 in which initial garnet crystals are reduced to tiny residual grains ($< 1$ vol %) dispersed inside their products of destabilization (G2-Figs. 3 and S3). However, the Grt initial shape was probably rounded to ovoid (e.g., G3; Figs. 3 and S4). Considering both the volume of reaction coronas and their current modal proportions, the initial Grt content was likely between 20 vol % and 25 vol % in the QFG.

The destabilization coronas around Grt involve Opx, Sp, minor iron–titanium oxides [$ITO = Il + Ti$-magnetite (TM)], and subordinated plagioclase and quartz (Figs. 5a and S2). Coronas of samples G2 and G3 involve tiny greyish patches of entangled microcrystals of Qz, feldspars, and black osumilite. Osumilite is usually in contact with Plg and its composition ($SiO_2 = 46\% \pm 5$, $Al_2O_3 = 23\% \pm 2$, $FeO = 21\% \pm 2$, $MgO = 3.3\% \pm 1.3$, $CaO = 2.8\% \pm 0.9$, $Na_2O = 1.3\% \pm 0.3$, and $K_2O = 1.3\% \pm 0.1$; Table S3) is close to the Ca-rich Os initially described by Miyashiro (1956; $SiO_2 = 48.3\%$, $Al_2O_3 = 22.1\%$, $FeO = 13.5\%$, $MgO = 9.1\%$, $CaO = 5\%$, $Na_2O = 0\%$, and $K_2O = 0\%$). The modal proportion of Opx (5 vol %–10 vol %) in garnet coronas, determined using EBSD mapping, is likely underestimated because most crystals forming these reaction coronas (Fig. 5) are too small ($\leq 50$ μm) and imbricated with smaller Sp grains (10–20 μm) to be correctly indexed at the scale of a thin section. Orthopyroxene crystal shape is essentially acicular; they are greenish to brown in color,
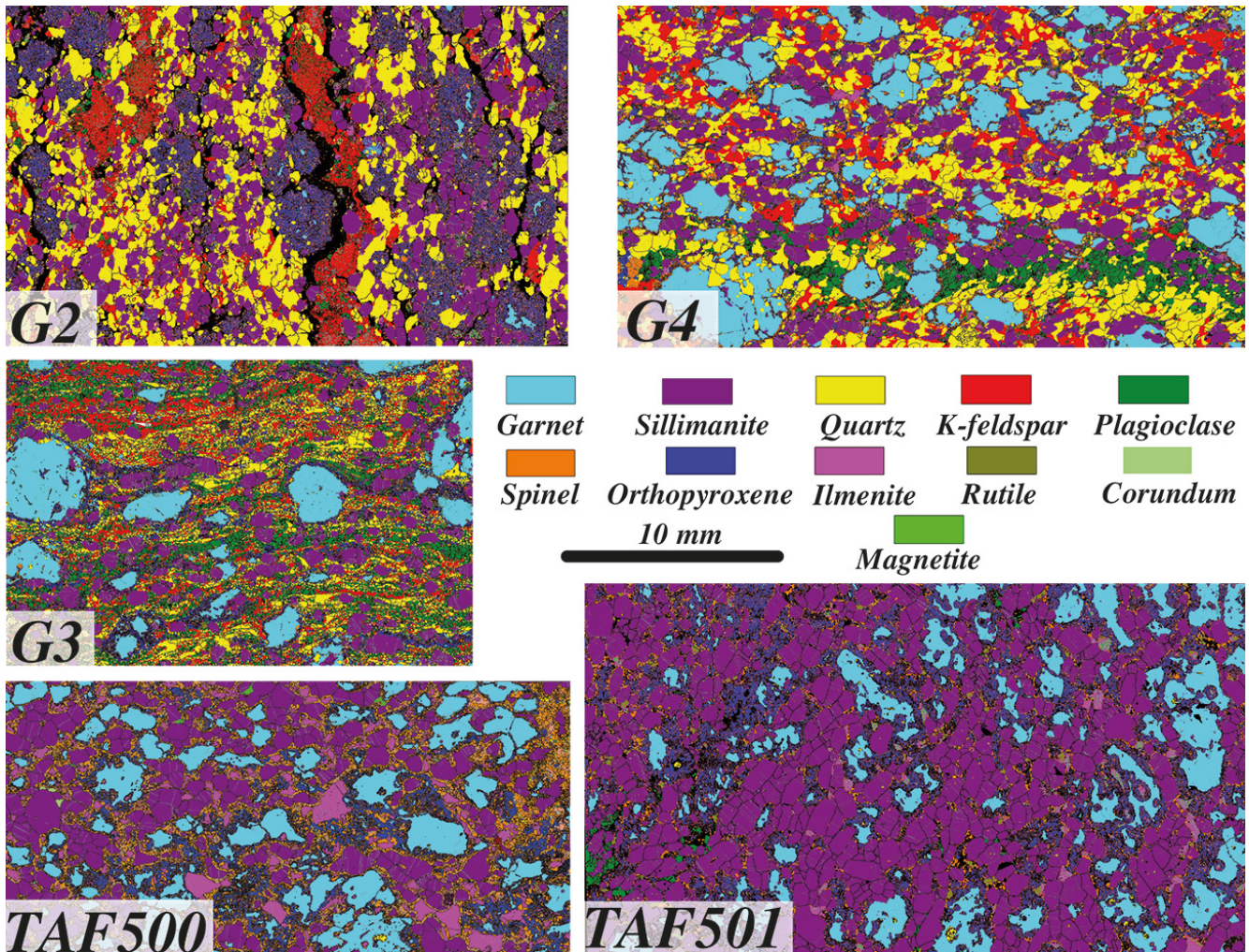
**Figure 3.** EBSD maps of the five selected granulite samples. All maps are at the same scale. The variation in the map size only depends on the mapped area. Samples G2 and TAF500 have been cut perpendicular to the foliation and also to the lineation (YZ plane), while G3, G4, and TAF501 have been cut perpendicular to the foliation and parallel to the lineation (XZ plane). Osumilite, although present in a low proportion in the quartzo-feldspathic samples, is not represented in the maps because the crystals are too small in size. Individual maps are available in the Supplement (Figs. S3 to S7).

**Table 1.** Modal proportions of rock-forming minerals for all selected granulites. The values have been evaluated from EBSD maps. The "not indexed" component includes glass, fractures, and crystals too small to be correctly indexed, such as some orthopyroxene, spinel, and quartz in garnet kelyphitic coronas. Tiny osumilite grains were detected in quartzo-feldspathic granulites but in proportions that are too small to be included in the mode. Small grains of corundum have been found only in the restitic granulite TAF500.

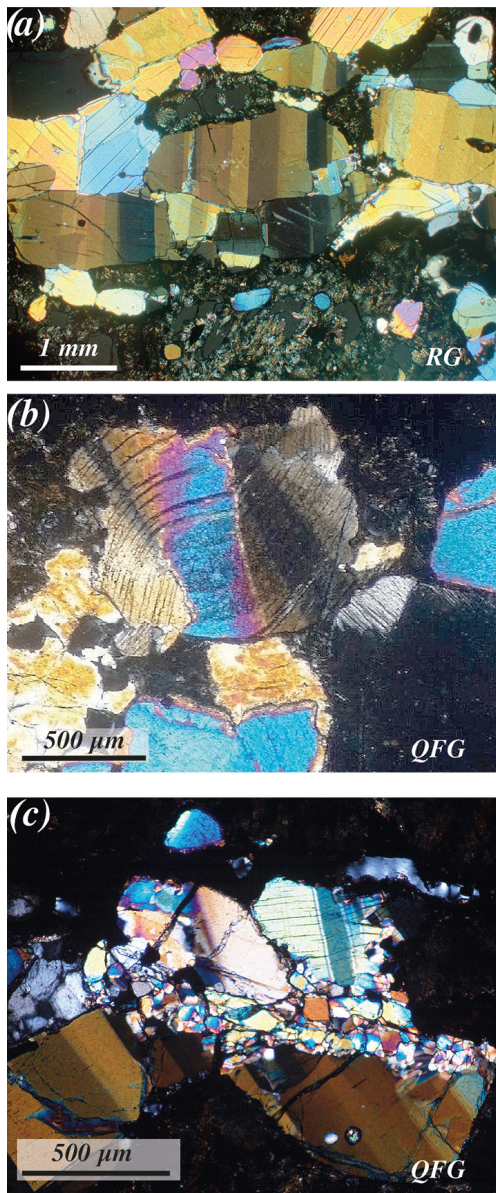| Samples | G2 | G3 | G4 | TAF500 | TAF501 |
|---|---|---|---|---|---|
| Grt (vol %) | 0.5 | 13 | 18.8 | 18.6 | 14 |
| Sil (vol %) | 25 | 18 | 23.4 | 28.2 | 46 |
| Qz; Pl; KF (vol %) | 25.4; 2.8; 11.3 | 15; 17; 9.8 | 22.1; 7.2; 8.7 | 3.3; < 0.1; 0 | 0.8; 0.8; < 0.1 |
| Opx; Sp (vol %) | 9.8; 9.6; | 6; 5.9 | 4.6; 8.4 | 10.2; 19 | 13.3; 8.6 |
| Rt; Il; TM (vol %) | < 0.1; 1.5; 0.5 | 0.6; 0.4; 0 | 0.2; 2.1; 0.4 | < 0.1; 8.6; 0 | 1; 1.9; 0.4 |
| Not indexed (vol %) | 14 | 18.1 | 4.5 | 12 | 14 |

**Figure 4.** Pictures of deformed sillimanite grains in polarized–analyzed light. **(a)** In TAF501, crystals show subgrain boundaries perpendicular to the lineation and to the [001] axis of the crystals. **(b)** In G3, a twisted crystal shows the initiation of recrystallization along the kink planes. **(c)** In G3, dynamic recrystallization of small new grains in parent crystals shows subgrain boundaries.



**Figure 5.** Detailed EBSD maps showing destabilization coronas around garnet **(a)** in the quartzo-feldspathic granulite G3 ($\sim$ 100–150 $\mu$m wide) and **(b)** in the restitic TAF501 ($\sim$ 1 mm wide). In G3, the garnet displays corrosion embayments and is surrounded by a first rim of tiny plagioclase grains (green) along its boundary then by a second rim corresponding to a mixture of spinel (orange grains) and orthopyroxene (blue). In TAF501, garnets also display embayments, and the coronas around them only involves orthopyroxene, spinel, and scarce minute quartz grains (yellow). Sillimanites (purple) are surrounded by a necklace of spinel and quartz, and ilmenite (fuchsia) contains relics of rutile (light green) and the exsolution of magnetite (orange lamellae). In both maps, domains in black are not indexed.

with a well-marked pleochroism. Their compositions are significantly variable within each individual sample but, on average, quite similar from one sample to another (Table S4). For instance, in the case of Opx in kelyphite around garnet, the FeOTotal average content is 28.5 % ($\sigma = 0.7$) in G2, 27.8 % ($\sigma = 2.4$) in G3, and 27 % ($\sigma = 1.7$) in G4, and the Al$_2$O$_3$ average content is 11.9 % ($\sigma = 0.5$) in G2, 11.1 % ($\sigma = 3.8$) in G3, and 13 % ($\sigma = 2.8$) in G4. Such high Fe and Al contents suggest that Opx result from Grt breakdown
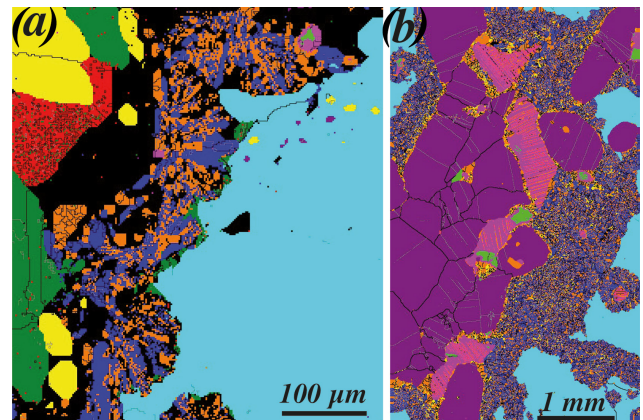
under high-temperature conditions (Harley, 1998). The $X_{FeTotal}$ (FeT/FeT + Mg) varies from 0.4 to 0.61. The Fe$_2$O$_3$ content of Opx in the kelyphitic coronas computed using the method in Schumacher (1991) is variable but low; the ratio ($100 \times Fe^{3+}/Fe^{2+}$) reaches 15 at most, except for one Opx in the glass in G3 which reached 27 (Table S4).

Dark-brown to black small spinel grains are present in all quartzo-feldspathic samples (6 vol %–9.5 vol %) and are most often dispersed inside the destabilization coronas around Grt (Fig. 5a). These Sp are hercynite solid solutions ($X_{FeTotal} = 0.57$–0.75; Al$_2$O$_3 = 51$ wt %–62 wt %; Table S5), always with low contents of TiO$_2$ + Cr$_2$O$_3$ + MnO + ZnO ($< 2.7$ %). The $X_{Fe2+}$, computed using the Droop (1987) method, lies between 0.77 and 0.95. In addition, in sample G2, Sp grains form discontinuous necklaces around Sil crystals.

Accessory minerals in the Tafraoute QFG consist of rutile (Table S6), ilmenite (Table S7), graphite, and zircon, as in Beni Bousera. The most abundant is ilmenite (0.4 vol %–8.6 vol %). Minute crystals of rutile (0.1 vol %–0.6 vol %) are also dispersed through the rock, and some are included in garnets; they contain $\sim$ 99 % of TiO$_2$, $< 0.6$ % of (Al$_2$O$_3$ + Fe$_2$O$_3$) and 2630 ppm of Zr in G2. Graphite is both dispersed in the rock and included in garnet. Zircon occurs in the matrix and is also present in garnet coronas, but it is absent inside the garnet.

Glass in G2 appears as small patches inside garnet coronas and has a rather homogeneous composition ($SiO_2 \sim 63\%$; ($Na_2O + K_2O$) $\sim 6\%$; $Al_2O_3 \sim 15\%$; $FeOTotal \sim 10\%$; $MgO \sim 1.3\%$; $CaO \sim 0.5\%$; Table S8). Glass is less abundant in G3 and G4 and relatively richer in CaO ($\sim 5\%$ and $6.5\%$, respectively) and in FeOTotal ($\sim 14\%$ and $17\%$), and it is poorer in alkalis ($Na_2O + K_2O = 2.5\%$ and $0.5\%$, respectively) in $SiO_2$ ($56\%$ and $53\%$), while Al and Mg contents are almost similar (Table S8).

In the QFG, the chemical composition of K-feldspars is relatively homogeneous ($0.72 < X_{or} < 0.82$; $0.16 < X_{ab} < 0.26$; Table S9). In contrast, the composition of plagioclases is variable from one sample to the other (Table S9); for G2 and G3, $X_{an}$ falls between 0.32 and 0.42. In G2 $X_{ab}$ is comprised between 0.37 and 0.57, and it is 0.61 in G3. In these two samples, $X_{or}$ values are close ($0.06 < X_{or} < 0.11$), except for two analyses in G2 ($X_{or} = 0.17$ and 0.27). In G4, plagioclases are richer in Na ($X_{ab} \sim 0.8$) and poorer in Ca ($X_{an} \sim 0.2$), with $X_{or}$ values around 0.05.

Various microstructures can be defined from quartz and feldspars (Fig. 3). Sample G2 (Qz 25 vol %, KF 11 vol %, and Plg 2.8 vol %; Table 1; Fig. 3) differs in the presence of almost monomineralic aggregates (1–2 mm thick) of K-feldspars parallel to the foliation, involving coarse and fine grains. The coarsest grains (up to 5 mm) are highly perthitic lenticular porphyroclasts displaying undulose extinction and surrounded by polyhedral smaller grains (0.2–0.5 mm) free of internal microstructure. These smaller grains display frequent 120° triple junctions and are generally free of perthitic exsolution; they have the same composition as the large KF crystals between exsolutions. Tiny grains ($\sim 100\,\mu m$) of plagioclase crystallized between these smaller KF, either along their boundaries or at triple junctions. In addition, a few larger grains (up to 500 $\mu m$) of plagioclase (Ab57, An35, and Or8) are dispersed in KF aggregates. Quartz is rather abundant in this sample; it appears mostly as large and usually elongated xenomorphic crystals (up to 2.5 mm long), forming quartz-rich domains between K-feldspar and sillimanite-rich layers. Some large grains display a weak undulose extinction, but there is no evidence of annealing.

In sample G3 (Qz 15 vol %; KF 10 vol %; Plg 17 vol %; Table 1; Fig. 3), in addition to the preferred shape orientation of sillimanite, the foliation is underlined by more or less continuous, almost monomineralic, layers (0.5–2 mm thick) of fine- to medium-grained plagioclase (100–500 $\mu m$) or quartz (100–700 $\mu m$), both showing a tendency towards polygonal shapes. Locally, quartz forms ribbons up to 5 mm long in which quartz grains display a rectangular shape (platten quartz; G3 Fig. 3), suggesting grain boundary migration. In sample G3, but also in G4, quartz locally fills embayments and cracks in garnet, suggesting the late percolation of a Si-rich fluid phase. KF grains ($< 250\,\mu m$) are locally included within Plg or Qz layers. In addition, discontinuous necklaces of tiny plagioclase grains ($\sim 10\,\mu m$) occur between
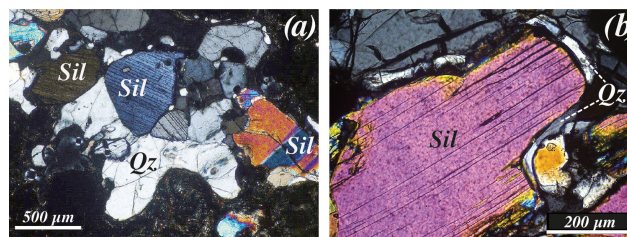


**Figure 6.** Pictures in polarized–analyzed light of undeformed interstitial quartz crystal **(a)** and quartz films around sillimanite **(b)** in sample G4.

garnets and their surrounding corona. A peculiarity of G3 is the presence of Qz, KF, and Plg as micro-inclusions within some garnets. The composition of these Plg ($X_{an} \sim 0.34$, $X_{ab} \sim 0.58$, and $X_{or} \sim 0.09$) is faintly poorer in Na compared to the one of Plg outside Grt ($X_{an} \sim 0.33$, $X_{ab} \sim 0.61$, and $X_{or} \sim 0.07$), while compositions of KF (Table S9) are almost similar ($X_{or} \sim 0.77$; $X_{ab} \sim 0.2$; $X_{an} \sim 0.02$).

Sample G4 (Figs. 3 and S5; Qz 22 vol %; KF 9 vol %; Plg 7 vol %; Table 1) displays a rather homogeneous microstructure. In this sample, quartz grains (50–200 $\mu m$) are free of intracrystalline substructure; they are either dispersed or concentrated in layers up to 3 mm wide. In these layers, quartz crystals are frequently elongated with their long axes oblique to the foliation (Fig. 3). The largest quartz grains have an interstitial habitus (Fig. 6a), while smaller ones display a polygonal shape with frequent 120° triple junctions. In addition, narrow films ($< 10\,\mu m$ wide) of quartz occur along boundaries of some sillimanite and feldspars (Fig. 6b). As in G3, most garnets display embayments and fractures filled either by microgranular quartz or Opx and Sp or by a mixture of these three minerals. Millimeter-sized aggregates of KF and Plg ($X_{ab} = \sim 0.77$; $X_{an} = \sim 0.18$; $X_{or} = \sim 0.05$) interstitial grains are locally dispersed within Qz aggregates. This network wraps both garnets ($\leq 6$ mm) surrounded by reactional coronas as in G3 and prismatic sillimanite. Altogether, these observations support a late percolation of a Si-, Na-, and K-rich fluid phase throughout the rock, and its crystallization in pores and along grain boundaries, evoking the microstructures described by Holness and Sawyer (2008).

## 4.2 The restitic granulites (RGs)

Restitic granulites (Fig. 2b) differ from the QFGs by the presence of (1) a higher abundance of sillimanite than in QFGs, but these sillimanites display similar chemical compositions (Table S1) and also evidence of intracrystalline deformation as in QFGs, (2) a widespread anastomosed network of Opx and Sp, (3) low proportions (vol % < 4) and small sizes of quartz and feldspars, and (4) many large pockets (up to 1 mm) of brown glass locally forming a diffuse network superimposed to the Opx and Sp network. In TAF501, Sil crystals (46 vol %; Table 1) are contiguous and display

an elongated prismatic shape (up to 3 mm long and 1 mm wide). As supported by crystallographic orientation measurements presented in Sect. 5, these Sil crystals display a CPO defining the foliation and lineation. Most Sil crystals are surrounded by discontinuous girdles of spinel ($\sim 50 \, \mu$m in size) and quartz (10–20 $\mu$m) grains, suggesting a destabilization of Sil and leading to the crystallization of these two phases (e.g., Figs. 3 and 5b). In TAF500, when Sil crystals form aggregates, Sil–Sil boundaries are rather rectilinear, locally with 120° triple junctions and free of evidence of destabilization (Figs. 3 and S6). On the contrary, external boundaries are polylobate and display embayments. In this sample, continuous coronas of Sp (100–300 $\mu$m) and Qz (20–50 $\mu$m) grains systematically wrap Sil isolated crystals and aggregate, and this mixture also fills their embayments (Figs. 3 and 5). The largest embayments are frequently neighboring ilmenite crystals, and Sp + Qz coronas also surround these ilmenite crystals, suggesting that ilmenite is involved in the destabilization of Sil. Locally, small grains of corundum ($\leq 350 \, \mu$m, $Al_2O_3 = \sim 97.5 \, \%$, and $FeO = \sim 2 \, \%$; Table S10) are alongside sillimanite boundaries and even fill embayments. This supports the idea that, locally, the Sil destabilization may have generated Crn through the reaction Sil Crn + Qz. According to Guiraud et al. (1996a), Ouzegane et al. (2003), and Diener and Powell (2010), this reaction occurs at temperatures between 800 and 1100 °C under pressure near 1 GPa.

In both studied TAF500 and TAF501, garnets are plurimillimetric to centimetric in size and have chemical compositions similar to those in the QFG samples ($X_{alm} = 0.51$ and 0.56, respectively; $X_{pyr} = 0.41$ and 0.36; $X_{sps} = 0.02$; $X_{grs} = 0.05$ and 0.06; and $X_{Fe2+} = 0.56$ and 0.61; Table S2). In addition, they display a skeletal shape resulting from intense corrosion. In TAF501, Grt are surrounded by an anastomosed microgranular network composed of Opx (100–300 $\mu$m) and spinel ($\sim 50$–250 $\mu$m) anhedral grains mixed with tiny quartz grains ($\leq 30 \, \mu$m). This mixture locally occurs between sillimanite grains. In TAF500, the anastomosed network has the same mineral composition but differs by the size and shape of Opx that surround residual garnets. Orthopyroxene (10.2 vol %) mostly appears as large poikilitic monocrysts (> 0.5 cm; Fig. 7). These monocrysts display extremely irregular shapes, with some of them sprawling between sillimanite, ilmenite, and/or garnet crystals (Fig. 7). Such a habitus suggests an interstitial crystallization, possibly from a liquid. The composition of Opx around garnet in both RGs (Table S4) falls in the same variation domain as for QFGs. Their averaged $Al_2O_3$ content is 13.7 ($\sigma = 1.9$) in TAF500 and 11.5 ($\sigma = 1.5$) in TAF501. The averaged FeO content is 24.6 ($\sigma = 0.7$) in TAF500 and 27.4 ($\sigma = 0.9$) in TAF501. The averaged $X_{FeT}$ is 0.43 for TF500 and 0.51 for TAF501.

TAF500 is free of K-feldspar and plagioclase, while TAF501 locally contains some grains of plagioclase (0.8 vol %; 50–250 $\mu$m; Table 1), with $X_{an}$ varying between 0.22 and 0.39 (Table S9). Opaque minerals proportions vary

significantly between the two selected RGs (Table 1); in TAF500, there is only Il ($\sim 8.6$ vol %), and in TAF501, there is Rt + Il + TM (respectively, 1 vol %, 1.9 vol %, and 0.4 vol %). In these samples, opaque minerals are either dispersed between sillimanite and garnet or embedded in the fine-grained mixture forming the anastomosed network. Zirconium content in rutile varies between 1900 and 2350 ppm, but there is no significant variation between the core and rim of single crystals. In TAF501, ilmenite appears as small-to-medium-sized anhedral crystals scattered throughout the rocks (Fig. 3). The largest crystals (up to 1 mm) frequently contain residual cores of rutile ($\leq 250 \, \mu$m) and exsolution lamellae of Ti-magnetite (Fig. 5b). When ilmenite is in contact with the kelyphitic coronas of garnet, it displays embayments and is bounded by a continuous strip of Ti-magnetite ($\sim 10 \, \mu$m wide). In TAF500 (Figs. 3 and S6), ilmenite crystals are larger (up to 2 mm) and are free of TM exsolutions. As stated above, these crystals are usually surrounded by Sp aggregates and, thus, separated from Sil or Opx.

Brown glass ($\pm$ vesicular; Fig. 8) appears as ameboid pockets (estimated vol %: 5–10) in the two RGs (up to 1.5 mm wide in TAF500 and 0.5 mm in TAF501). Compared to glasses of QFGs, those found in the RGs are relatively richer in FeO, MgO, and $TiO_2$ and less rich in $SiO_2$, $Na_2O$, and $K_2O$ ($SiO_2 \sim 48 \, \%$ in TAF500 and $\sim 52 \, \%$ in TAF501; $Na_2O + K_2O \sim 0.2 \, \%$ and $\sim 0.65 \, \%$; $Al_2O_3 \sim 16.4 \, \%$ and 16.1 %; FeOTotal $\sim 18.5 \, \%$ and $\sim 20.2 \, \%$; MgO $\sim 3 \, \%$ and $\sim 2.8 \, \%$; CaO $\sim 5.8 \, \%$ and $\sim 4.8 \, \%$; Table S8). Fibroradiated aggregates (up to 600 $\mu$m) of acicular Opx ($\pm$ minute spinel and quartz), centered either on an opaque grain or a patch of residual brown glass, are present in both RG samples (Fig. 8). Such a microstructure suggests spherulitic crystallization of a glass. In addition, in TAF500, some larger crystals of Opx in contact with glass pockets show overgrowth leading to the formation of idiomorphic terminal faces inside glass.

### 4.3 Corundum megacrysts

A peculiarity of Tafraoute tuffs is the presence of hexagonal tablets of dark blue to black corundum idiomorphic megacrysts (up to 3 cm in diameter and 1 cm thick; Fig. 9a). Such crystals have not been encountered in the studied granulite xenoliths where corundum was only observed in the refractory granulite TAF500 as small (< 200 $\mu$m) xenomorphic and interstitial crystals. A few megacrysts have clean flat faces, while most of them display more or less irregular faces due to the presence of corrosion cavities often filled with brown palagonite. In thin section, although the crystals appear irregularly colored (Fig. 9b), their cores are generally more intensely colored (light blue to slightly purplish) than their rims which additionally appear always darkened (Fig. 9b). Furthermore, they display multidirectional polysynthetic twins (Fig. 9c), and they are deformation-free but strongly fractured, especially at their peripheries (Fig. 9b). Face corrosion, fracturing, and rim darkening are
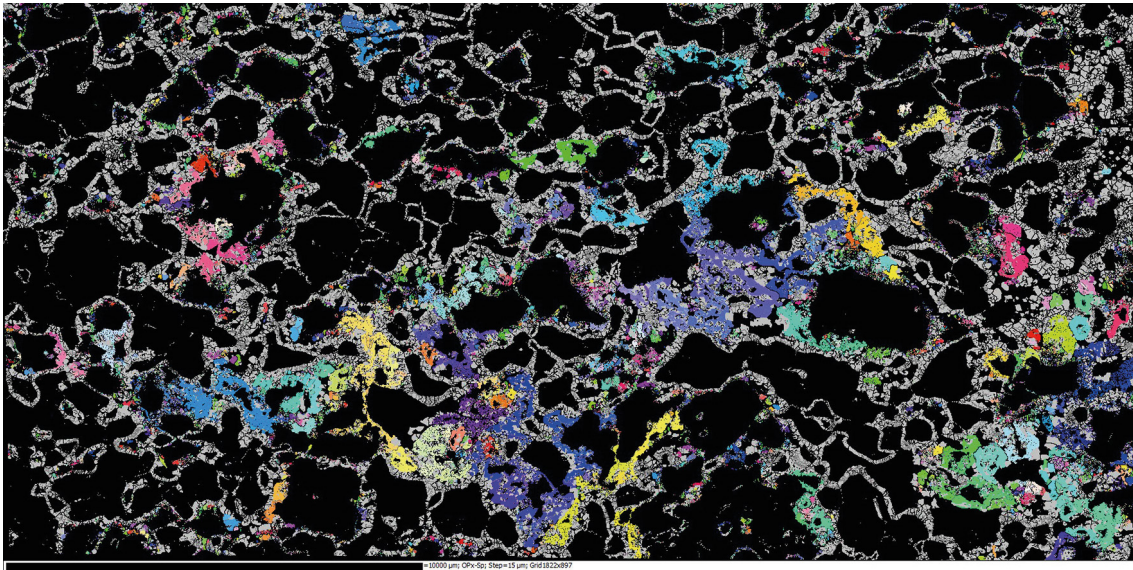
**Figure 7.** Detailed EBSD map of restitic granulite TAF500. All constitutive minerals are in black, except spinel in grey, while all other colors correspond to orthopyroxene. These colors depend on the crystallographic orientation (Euler angles) of each Opx crystal. This map reveals the habitus of small grains of spinel that form coronas around sillimanite and ilmenite and the peculiar habitus of Opx. The uniformity of color (and, thus, of crystallographic orientation) over large areas substantiate that most Opx crystals are rather large in size and undeformed. Their sprawling habitus and the abundance of spinel and sillimanite inclusions support an interstitial to poikiloblastic crystallization.
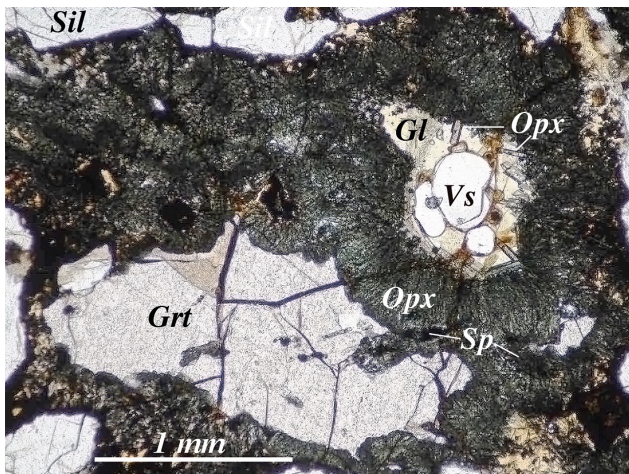


**Figure 8.** Microphotograph of a vesicular glass pocket (TAF501) in the center of a fibroradiated aggregate of orthopyroxene (Opx). Gl = glass; Grt = garnet; Sil = sillimanite; Sp = spinel; Vs = vesicle.

likely consequences of their transport in lava from their place of origin to the surface.

One megacryst, selected for its size (1 cm) and transparency (Fig. 9), has been analyzed for major and trace element (Table S10). Its Al and Fe contents seem slightly higher at the core ($Al_2O_3 = \sim 98\%$ and $FeO = 2.1\%$) compared to the rims ($\sim 97$ and $1.7$). Note that these Fe contents are slightly higher than that of the interstitial corun-

dums of restitic sample TAF500 ($0.9 < \% FeO < 1.1$). This megacryst contains anhedral micro-inclusions of titanomagnetite ($TiO_2 = \sim 20\%$; Table S10) and sillimanite grouped in a small millimetric cluster and with compositions close to those encountered in refractory xenoliths. In addition, a small Opx crystal with very high Al contents ($Al_2O_3 = 22.5\%$) is stuck on one face of the corundum megacryst (Table S10). Such very high Al content is uncommon (to our knowledge, they have been found only once in Opx from Indian Eastern Ghats province pelitic granulites; Bhattacharya and Kar, 2002). In our case, this anomalously high Al content might result from contamination of Opx by the contiguous corundum. However, this Al content is close to those measured in some Opx encountered inside the kelyphitic corona of G3 garnets ($18.6\%$) or in the glassy thin coating around kelyphitized garnets in G2 sample ($Al_2O_3$ up to $19.3\%$), which are two samples that are corundum free.

The origin of the Tafraoute corundum megacrysts is problematic; is it magmatic or metamorphic? The origin of magmatic corundum from basalts has been discussed in several articles (e.g., Peucat et al., 2007; Uher et al., 2012, and references therein). All authors consider that, in addition to Fe, Mg, Ti, and Cr contents, the Ga content is essential for determining corundum origin. Peucat et al. (2007) even demonstrated that the Ga/Mg ratio, in conjunction with the Fe concentration, is an efficient tool to discriminate metamorphic from magmatic corundum. To use this discrimination criterion, we carried out four laser ablation inductively coupled plasma mass spectrometry (LA-ICP-MS) analyses on the se-
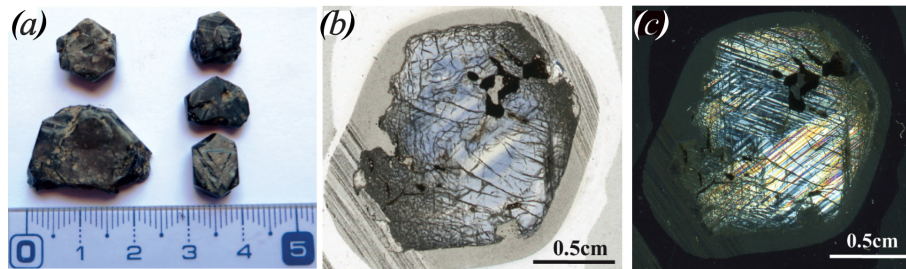
**Figure 9.** Corundum megacrysts from Tafraoute tuffs **(a)**. Microphotographs of the megacryst selected for analysis in plane-polarized light **(b)** and in cross-polarized light **(c)**. In panel **(a)**, the analyzed megacryst is the upper-left crystal.

lected megacryst (Fig. 9). Analytical procedures and analyzed results are available in Table S10.

According to Peucat et al. (2007), magmatic blue corundum found in alkali basalts are commonly medium-rich to rich in Fe (with average contents between 2000 and 11 000 ppm), high in Ga (> 140 ppm), and low in Mg (generally > 20 ppm), with high Ga/Mg ratios (> 10). The metamorphic blue sapphires are characterized by low average Fe contents (< 3000 ppm), low Ga contents (< 75 ppm), and high Mg values (> 60 ppm) with low average Ga/Mg ratios (< 10). The Tafraoute megacryst has a high Fe average content of 14 770 ppm ($\sigma = 1470$) and it is also Ga-rich (325 ppm, $\sigma = 19$); its Mg content is very variable (53 ppm; $\sigma = 53$) and its Ga/Mg ratio is consequently variable but relatively low (six on average) and therefore lower than those proposed by Peucat et al. (2007) for the magmatic corundum. Its average contents in Ti and Cr are 459 ppm ($\sigma = 159$) and 196 ppm ($\sigma = 80$), respectively. In the binary Fe – Ga/Mg and the triangular (Fe − Mg × 100 − Ti × 10) diagrams proposed by Peucat et al. (2007), our megacryst plots in the magmatic field but close to the metamorphic field limit. In the diagrams (Cr × 10 – Ga/Mg × 100) of Sutherland et al. (1998) that are modified by Uher et al. (2012), it plots in the metamorphic field. These first results obtained on only one sample suggest a possible origin that is both metamorphic and magmatic for the Tafraoute corundum megacryst.

# 5 Crystal-preferred orientations (CPOs)

The crystallographic-preferred orientation of the main constitutive minerals of the five selected granulite samples have been analyzed using EBSD measurements.

## 5.1 Restitic granulites (Figs. 10 and S8)

In TAF500 and TAF501, only Sil, Grt, and Opx are abundant enough to provide reliable CPO measurements. The large sillimanite crystals display substructures typical from dislocation creep and have developed a moderate but well-defined crystallographic fabric. The presence of weakly deformed or even undeformed small grains may weaken the

fabric strength of sillimanite. The CPO is characterized by a concentration of [001] axes around a direction parallel to the foliation and [100] and [010] dispersed in a wide girdle normal to the maximum of [001]. This girdle contains a weak concentration of [100] and [010] normal to the foliation plane. This [001] fiber CPO type, together with the presence of subgrain boundaries normal to [001], suggests the dominant activation of the [001] dislocation glide possibly on both the (100) and (010) slip planes (e.g., Piazolo and Jaconelli, 2013). However, participation of oriented crystallization or inheritance from pre-existing kyanite crystals to the formation of this preferred orientation cannot be ruled out.

Garnets are almost randomly oriented and no CPO can be defined. They show several point concentrations with no correlation between them (see Fig. S8), which are likely due to the separation of original crystals in several pieces resulting from fracturing and garnet breakdown.

Opx [100] and [001] only display weak concentrations without any correlation with the sillimanite CPO.

## 5.2 Quartzo-feldspathic granulites (Figs. 10 and S9)

Sillimanite crystals also display a weak but well-defined CPO similar to the one in the restitic granulites. This fabric likely results from the ductile deformation at the origin of the intragranular microstructure and dynamic recrystallization of large sillimanite crystals, as previously described.

Quartz, in samples G2 and G3, displays a weak concentration of [0001] in a direction oblique to the main concentration of [001]sil, and the <a> and <m> axes tend to form girdles corresponding to a dispersion around a plane normal to the main concentration of [0001]c (Fig. 10). In sample G4, the quartz CPO is more random and not reliably interpretable (Fig. S9). This weak fabric might be due to either a faint deformation through the activation of the <a> slip direction on prismatic planes or to oriented crystallization from a percolating melt.

K-feldspar and plagioclase crystals display nearly random orientation, even when they form almost monomineralic layers. This lack of preferred orientation, consistent with the frequent interstitial habitus of these phases, points to a late crystallization from a percolating melt.
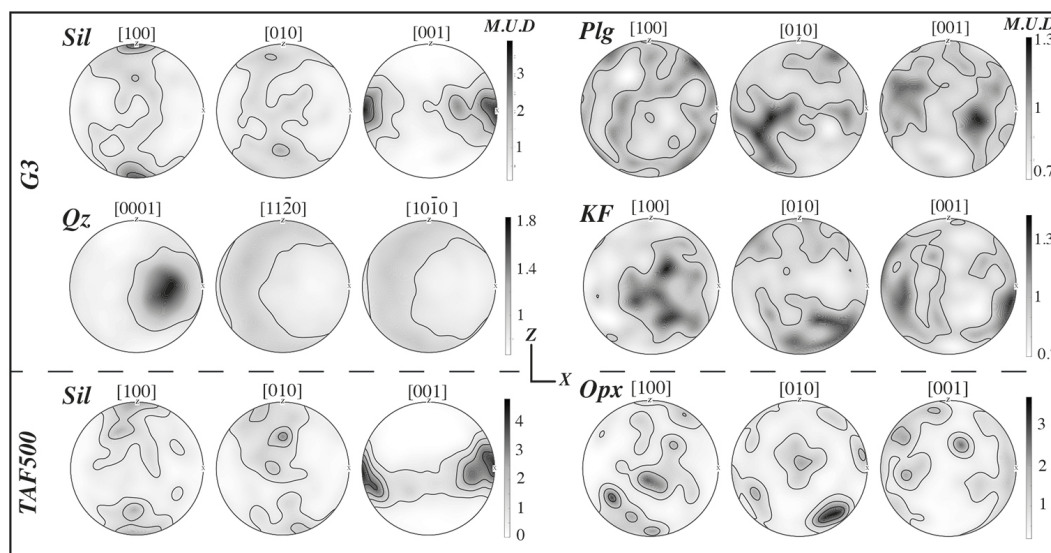
**Figure 10.** Representative crystallographic-preferred orientation (CPO) of **(a)** sillimanite, quartz, K-feldspar, and plagioclase in the quartzo-feldspathic granulite G3. **(b)** Sillimanite and orthopyroxene in the restitic granulite TAF500. Lower-hemisphere stereographic projections with contours at one multiple of a uniform distribution (MUD) interval. The greyscale corresponds to MUD for each cell. To facilitate comparisons, CPOs have been rotated to put [001] of sillimanite in the E–W direction, considering that the maximum concentration of this axis is representative of the lineation. The foliation is $\sim$ E–W and normal to the plane of the pole figure. In both samples, sillimanite displays a clear preferred orientation, despite a weak dispersion of [001] in the foliation plane. In G3, feldspars do not show any reliable preferred orientation, and quartz displays a weak one without correlation with the CPO of sillimanite. In TAF500, orthopyroxene is randomly oriented. Additional data are available in Figs. S8 and S9.

## 6 Geothermobarometry

Considering the mineralogical and microstructural characteristics of the Tafraoute granulites, only garnet core with its inclusions (rutile, ilmenite, graphite, plagioclase, and K-feldspar) and the core of KF porphyroclasts in G2 can be reliably considered belonging to a primary paragenesis. Due to its prismatic habitus and the presence of 74° cleavages in some crystals, sillimanite probably results from later polymorphic transformation of primary kyanite. In this hypothesis, primary paragenesis of the Tafraoute and Beni Bousera granulites might have been similar. According to El Maz and Guiraud (2001) estimates, the $P$ and $T$ equilibrium conditions of Beni Bousera granulites reached 1–1.3 GPa and 800–870 °C. In this hypothesis, the granulites from Tafraoute would have been initially equilibrated at a depth of $\sim$ 35–40 km, close to the limit between the kyanite and sillimanite stability field. On the other hand, Opx and Sp coronas observed in the Tafraoute samples are probably the products of a later destabilization of garnet through the reaction Grt + Sil/Ky $\rightarrow$ Al–Opx + Sp $\pm$ Plg $\pm$ Qz (Figs. 5 and S2) and will be considered representing a second paragenesis. Quartz and feldspars from the matrix display evidence of late remobilization and recrystallization possibly related to partial melting. The glass, and thus the spherulitic Opx around glass pockets, likely results from the fast melting (flash melting) of rocks triggered by their entrapment and ascent in lavas, followed by fast cooling at the surface.

### 6.1 Equilibrium conditions for the primary paragenesis (P I) (Table 2)

The lack of biotite in the studied samples excludes the application of garnet–biotite to estimate $P$ and $T$ conditions corresponding to the first paragenesis. It is also not possible to use the feldspars pairs in the matrix because they likely were remobilized during their subsequent evolution. However, the garnets in sample G3 include plagioclase, K-feldspar, rutile, quartz, ilmenite, and graphite, which can be used to estimate the temperature and pressure corresponding to the $P$ and $T$ conditions of the primary paragenesis.

#### 6.1.1 Pressure

The mineralogical assemblage of garnet–plagioclase–aluminosilicate–rutile–ilmenite–quartz is well known for its geobarometric potentiality. Several barometers and calibrations have been proposed for this assemblage, but they are all sensitive to temperature. Considering the lack of biotite in the primary paragenesis of our samples, likely resulting from the total consumption of this mineral through fluid-absent melting (at temperatures ranging between 850–875 °C; Vielzeuf and Holloway, 1988), and the similarity with the Beni Bousera granulites (Fig. 11), a starting

**Table 2.** Summary of temperature (°C) and pressure (GPa) estimates for the primary paragenesis (P I) of G3 granulite, using garnet core and feldspars included in garnet. Temperature is calculated at 1.1 GPa and pressure at 870 °C. To calculate $P$ and $T$ conditions, we used the software of Wen and Nekvasil (1994; model of Nekvasil and Burnham, 1987), Putirka (2008), Yavuz and Yavuz (2022; model of Benisek et al., 2010, for ternary feldspars, namely albite, orthoclase, and anorthite), and the calibration of Price (1985). Pressures are calculated assuming a temperature of 870 °C, using the calibration of Caddick and Thompson (2008) and Essene's abacus (1989) for GASP and GRIPS barometers. The mixing models of Koziol and Newton (1989) and Newton and Haselton (1981) were used for garnet and plagioclase, respectively. In all samples, the stable aluminosilicate considered is kyanite. In Tables 2 and 3, the numbers indicated above each column correspond to the analyzes used to estimate $T$ and $P$. These analyses are given in the Supplement.

| Primary paragenesis: feldspars in garnet (G3) | | | |
|---|---|---|---|
| Temperature (°C at 1.1 GPa) | | | |
| Plg–KF | 17–14 | 18–21 | 20–10 |
| Price (1985) | 863 | 853 | 876 |
| Wen and Nekvasil (1994) | 895 | 846 | 859 |
| Putirka (2008) | 864 | 860 | 862 |
| Yavuz and Yavuz (2022) Ab/Or/An | | | |
| $T_{albite}$ | 864 | 871 | 890 |
| $T_{orthose}$ | 854 | 891 | 896 |
| $T_{anorthite}$ | 889 | 867 | 845 |
| Pressure (GPa at 870 °C) | | | |
| Plg–Grt | 17–36 | 18–48 | 20–17 |
| GRIPS (Essene, 2008) | 1.05 | 1.07 | 1.07 |
| GASP (Essene, 2008) | 1.18 | 1.2 | 1.22 |
| Caddick and Thompson (2008) | 1.00 | 1.03 | 1.04 |



**Figure 11.** $P$–$T$–$t$ diagram showing the primary (P I) and secondary (P II) parageneses of Tafraoute granulites from Middle Atlas (TAF MA) and Beni Bousera (BB-Rif). In the case of Rif granulites, the pressures and temperatures of the primary and secondary paragenesis have been determined using THERMOCALC program of Holland and Powell (1988), and the ellipses correspond to $2\sigma$ error. Kyanite–sillimanite transition according to Holdaway and Mukhopadhyay (1993).

mometers give temperatures in the range 850–880 °C (Table 2 and Fig. 11). These temperature estimates are similar to those obtained using the software of Yavuz and Yavuz (2022).

These $P$ and $T$ estimates are in good agreement with conventional petrogenetic grids (e.g., Vielzeuf and Holloway, 1988; Nair and Chacko, 2002, and references therein), showing the lack of biotite and the presence of rutile in the primary mineralogical assemblage. These results corroborate that these rocks were equilibrated within the stability field of kyanite near the kyanite-sillimanite phase boundary (Fig. 11).

## 6.2 Equilibrium conditions of the secondary paragenesis (P II) (Table 3)

Estimates of the temperature and pressure were obtained using the Opx–Grt geothermobarometer, considering the Opx from the coronas in contact with the rims of garnets. This geothermobarometer is based on the $Fe^{2+}$–$Mg^{2+}$ exchange equilibrium; therefore, the $Fe_2O_3$ content in the phases involved in these exchange reactions should be estimated. Hence, as mentioned above, the Schumacher (1991) method was used for the Opx.

### 6.2.1 Temperature

This thermometer is almost insensitive to pressure. Several calibrations (Harley, 1984; Aranovich and Berman, 1997, and Sudholz et al., 2022) have been used. With a reference pressure $\sim 1$ GPa, temperature estimates computed for all QFG and RG samples fall between 1020 and 1120 °C (Ta-

reference temperature of 850 °C can be used to estimate the pressure. In these conditions, the pressures obtained using the GRIPS (garnet–rutile–ilmenite–plagioclase–silica) and GASP (garnet–aluminosilicate–silica–plagioclase) abacus of Essene (1989), with garnet inclusions and the garnet core of sample G3 between 1.1 and 1.2 GPa (Table 2). The calibration of Caddick and Thompson (2008) for the GASP barometer provides pressures that are slightly lower, i.e., $\sim 1$ GPa at 850 °C (Table 2). These estimates are in good agreement with the Bohlen et al. (1983) experimental results carried out on the GRIPS assemblage (1.2 and 1.3 GPa at 850 and 900 °C).

### 6.1.2 Temperature

The binary feldspar thermometers (Price, 1985; Putirka, 2008), weakly sensitive to pressure, and ternary feldspar, using SOLVCALC 2.0 software (Wen and Nekvasil, 1994), can be applied to the two feldspars included in garnet. With the reference pressure of 1.1 GPa estimated above, these ther-
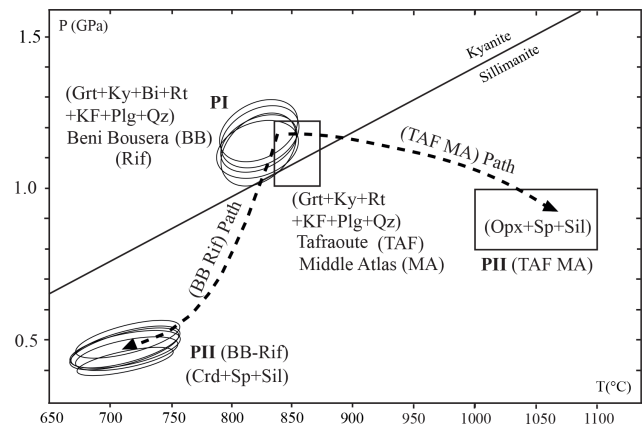
**Table 3.** Summary of temperature and pressure estimates for the secondary and tertiary parageneses (P II and P III). Temperature (°C) was calculated at an assumed pressure of 0.9 GPa and pressure at an assumed temperature of 1100 °C. P II was determined using Opx in contact with garnet rim. Garnet–orthopyroxene geothermobarometer taken from Harley (1984), Aranovich and Berman (1997), Sudholz et al. (2022), Harley and Green (1982), and Nickel and Green (1985). P III was determined using minerals in glass, with calibrations and programs using orthopyroxene–ilmenite (Charlier et al., 2007), orthopyroxene–spinel (Sato et al., 2012), orthopyroxene–glass (Beattie, 1993, and Eq. 28b of Putirka, 2008), silica activity in glass (Albarède, 1992), Fe–Ti oxides, and $Log_{10}$ ($f_{O_2}$) (ILMAT program from Lepage, 2003; Spencer and Lindsley (1981) calibration and Lindsley and Spencer model (1982) for the ulvöspinel and ilmenite molar fractions in the oxides). $Log_{10}$ ($f_{O_2}$) = $Log_{10}$ of oxygen fugacity.

**Paragenesis II**

| Samples | G2 | | G3 | | G4 | | TAF500 | | | TAF501 | | |
|---|---|---|---|---|---|---|---|---|---|---|---|---|
| Garnet–orthopyroxene | 15–10 | 64–13 | 9–54 | 8–8 | 70–66 | 62–56 | 1–7 | 4–15 | 64–6 | 9–38 | 36–23 | 77–24 |
| **Temperature (in °C) (at 0.9 GPa)** | | | | | | | | | | | | |
| Harley (1984) | 1114 | 1126 | 1093 | 1000 | 1153 | 1069 | 1091 | 1137 | 1079 | 1048 | 1136 | 1090 |
| Aranovich and Berman (1997) | 1117 | 1108 | 1089 | 1068 | 1123 | 1086 | 1086 | 1098 | 1064 | 1112 | 1092 | 1069 |
| Sudholz et al. (2022) | 1063 | 1071 | 1030 | 939 | 1107 | 1013 | 1080 | 1084 | 1020 | 1065 | 1089 | 1043 |
| **Pressure in GPa (at 1100 °C)** | | | | | | | | | | | | |
| Harley and Green (1982) | 0.76 | 0.78 | 0.75 | 0.82 | 0.74 | 0.77 | 0.77 | 0.77 | 0.77 | 0.82 | 0.80 | 0.76 |
| Nickel and Green (1985) | 1.04 | 1.06 | 1.20 | 1.05 | 0.91 | 0.91 | 0.96 | 0.96 | 0.98 | 0.93 | 1.05 | 1.05 |

**Paragenesis III**

| Samples | G2 | | G3 | | G4 | | TAF500 | | | TAF501 | | |
|---|---|---|---|---|---|---|---|---|---|---|---|---|
| **Temperature (in °C) (at 0.9 GPa)** | | | | | | | | | | | | |
| Orthopyroxene–ilmenite | 5–28 | | 13–26 | | | | 9–8 | 70–71 | | 2–42 | 76–41 | |
| Charlier et al. (2007) | 1032 | | 1029 | | | | 1094 | 1098 | | 1142 | 1080 | |
| Orthopyroxene–spinel | 16–34 | 32–71 | | | 18–63 | 67–61 | 31–45 | 68–72 | | 18–14 | 76–15 | |
| Sato et al. (2012) | 1070 | 1108 | | | 1091 | 1057 | 1131 | 1119 | | 1147 | 1065 | |
| Orthopyroxene–glass | 5–35 | 9–58 | 60-26 | | 9–15 | 10–7 | 9'–8 | 9–10' | 70–69 | 2–38 | 3–39 | 38–21 |
| Beattie (1993) | 1152 | 1086 | 1124 | | 1110 | 1115 | 1105 | 1120 | 1154 | 1157 | 1154 | 1172 |
| Equation (28b) (Putirka, 2008) | 1011 | 1012 | 1038 | | 1055 | 1049 | 1077 | 1114 | 1160 | 1117 | 1118 | 1122 |
| Glass (silica activity) | 35 | 58 | 26 | 30 | 7 | 15 | 8 | 10' | 69 | 21 | 38 | 39 |
| Glass (silica activity): Albarède (1992) | 1004 | 1011 | 1020 | 1047 | 1027 | 1030 | 1044 | 1071 | 1109 | 1074 | 1071 | 1072 |

**Oxides: $T$ °C and $Log_{10}$ ($f_{O_2}$)**

| Samples | G2 | | G4 | | TAF501 | |
|---|---|---|---|---|---|---|
| Ilmenite–titanomagnetite | 22–30 | | 59–55 | | 9–8 | |
| Spencer and Lindsley (1981) Lindsley and Spencer (1982) | 1160 | −7.99 | 1081 | −8.66 | 1181 | −8.46 |

ble 3). These values point to an increase in temperature after the primary paragenesis (Fig. 11). This temperature increase, corresponding to the breakdown of Grt, is consistent with the polymorphic transformation of kyanite into sillimanite.

### 6.2.2 Pressure

The Grt–Opx geobarometer used in this study is temperature sensitive, and therefore an error of 50 °C generates a variation of 0.14 GPa. Using the calibration of Harley and Green (1982) with the reference temperatures of 1050 and 1100 °C, the estimated pressures are 0.76 and 0.88 GPa, respectively (Table 3). With the Nickel and Green (1985) calibration at the same temperatures, relatively higher pressures were obtained (0.86–1.25 GPa respectively; Table 3). The assemblage osumilite, orthopyroxene, garnet, feldspars, sillimanite, and quartz (as in sample G3) is stable at $T > 850$ °C between 0.8 and 0.9 GPa (Harley, 2008, and references therein) and 0.7 and 0.85 GPa (Das et al., 2001). Therefore, for Tafraoute granulites, the pressure estimates obtained using Nickel and Green (1985) calibration are likely slightly overestimated. In this case, the temperature increase suggested by our estimates would be coeval, with a slight pressure decrease (from ∼ 1.1 to ∼ 0.9 GPa).

### 6.3 Temperature estimates using matrix K-feldspars and plagioclase (Table 4)

Quartz and feldspars from the matrix display evidence of late remobilization and crystallization possibly related to a partial melting event. The temperatures computed using Plg and KF of the matrix would therefore correspond to equilibrium conditions subsequent to those recorded by P II. Plg–KF temperatures were estimated from the exchange of Ca, Na, and K using the Price (1985) geothermometer and Wen and Neckvasil (1994), Putirka (2008), and Yavuz and Yavuz (2022) software. For the three QFGs analyzed in this study, temperature estimates between 720 and 830 °C have been obtained (Table 4). These values are significantly lower than those obtained for both primary and secondary parageneses; they might result from the cooling of the lower crust after the episode of heating recorded by the second paragenesis.

### 6.4 Temperature estimate for the RG glass formation and crystallization (Table 3)

The glass present in the studied xenoliths represent the last thermal event these granulites underwent. To estimate the temperature of this late event, we analyzed the glass and the minerals resulting from its partial crystallization (Opx, Sp, and ITO). The geothermometers used are Opx–Il (Charlier et al., 2007), Opx–Sp (Sato et al., 2008), Opx–glass (Putirka, 2008), silica activity in glass (Albarède, 1992), and iron–titanium oxides (ILMAT software; Lepage, 2003). This last geothermometer is independent of the pressure; the others are almost insensitive to the pressure since an error of 0.4 GPa causes an error of less than 35 °C. Most of the calculated temperatures at a reference pressure of 0.9 GPa fall in the range between 1020 and 1160 °C (Table 3). The corresponding calculated Log $f$O$_2$ values are tightly between $-8$ and $-8.67$ (Table 3), supporting the idea that the glass formation occurred under oxidizing conditions. These estimated conditions may therefore result from the incorporation of granulitic xenoliths in the host basaltic magma.

## 7 Discussion

Two types of Al-rich granulite have been defined among the xenoliths from the Quaternary Tafraoute maar: "refractory" (almost free from quartz and feldspars) and "quartzo-feldspathic" (up to 42 vol % quartz + feldspars). Both types contain prismatic sillimanite deformed through dislocation creep, with garnet surrounded by undeformed destabilization coronas of variable width. The coronas around garnets involve Opx, Sp, and minor Qz and Plg tiny crystals. This likely reflects the reaction Grt + Sil → Al–Opx + Sp, classically attributed to temperature increase (higher than 940 °C in the KFMASHTO system; Wheller and Powell, 2014). In addition, the quartzo-feldspathic granulites contain quartz,

plagioclase, and K-feldspar often concentrated in almost monomineralic layers.

In sample G2, K-feldspar layers contain eye-shaped perthitic porphyroclasts displaying evidence of intracrystalline deformation, surrounded by smaller K-feldspar polyhedral grains. These small grains are most often exsolution-free and likely result from dynamic recrystallization of porphyroclasts. This supports that these porphyroclasts (1) belong to the initial paragenesis and (2) underwent high-temperature deformation resulting in partial recrystallization of their rim. Samples G3 and G4 contain layers of plagioclases with a polygonal grain shape; this supports the idea that they were annealed and might also, at least partially, derive from primary crystals. However, as stated before, some K-feldspar and plagioclase grains, free of intragranular deformation, locally display interstitial habitus supporting a post-deformation crystallization from a melt.

In all QFG samples, quartz also displays contrasting shapes and habitus that likely represent (1) original large grains (e.g., G2); (2) annealed, possibly dynamically recrystallized smaller crystals, sometimes forming ribbons (e.g., G3); and (3) deformation-free interstitial quartz with irregular grain shapes (e.g., G2 and G4), which locally forms thin films between preexisting phases or infills garnet embayments and fractures (e.g., G4 and G3).

This variety of habitus and microstructure of feldspars and quartz likely results from several successive tectono-metamorphic events. These three phases were present in the initial paragenesis; then, during the subsequent heating event, they underwent crystal plastic deformation and partial melting at the origin of local percolation and interstitial crystallization. In such a scenario, the refractory granulites might represent domains where the quartzo-feldspathic components were almost totally melted and extracted.

The evolution of the Tafraoute lower crust proposed below is substantiated by both mineralogical observations and $P$–$T$ conditions estimated from successive parageneses recognized in the studied granulite samples (Fig. 11):

- The observation of cleavages typical of kyanite in some prismatic sillimanites, suggests that the granulites of Tafraoute were originally equilibrated in the kyanite stability field, such as those of Beni Bousera ($\sim 850$ °C and $\sim 1.2$ GPa). This interpretation is consistent with the $P$ and $T$ equilibrium conditions (1.1 ± 0.1 GPa and 850–880 °C) estimated from garnet and its inclusions (Rt + Il + Gph + KF + Plg + Qz). This suggests an initial depth of $\sim 40$ km for these granulites. Such conditions are compatible with fluid-absent melting, in agreement with the lack of biotite in the studied QFG samples. Considering the similarities with Beni Bousera granulites, these conditions likely correspond to the Hercynian orogeny (Fig. 11).

- $P$ and $T$ estimated from garnet and the phases resulting from its destabilization are $\sim 0.9 \pm 0.1$ GPa and 1050–

**Table 4.** Summary of temperature estimates (°C) calculated at 0.9 GPa using matrix K-feldspars and plagioclases for G2, G3, and G4 samples. KF64 is a large porphyroclast, and KF65, KF45, and KF60 are medium sized to small. Calibrations and software used are the same as in Table 2.

| | $T$ °C at 0.9 GPa | | | |
| --- | --- | --- | --- | --- |
| | G2 | | G3 | G4 |
| | Plg39–KF64 | Plg70–KF65 | Plg44–KF45 | Plg46–KF60 |
| Price (1985) | 1012 | 855 | 797 | 723 |
| Wen and Nekvasil (1994) | 1030 | 876 | 833 | 789 |
| Putirka (2008) | 834 | 854 | 827 | 789 |
| Yavuz and Yavuz (2022) | | | | |
| $T_{albite}$ | 1200 | 866 | 788 | 628 |
| $T_{orthose}$ | 1087 | 882 | 821 | 611 |
| $T_{anorthite}$ | 744 | 832 | 851 | 923 |

1100 °C, suggesting that the lower crust underwent a temperature increase of $\sim 200$ °C compared to the primary equilibrium temperature. This heating could have been coeval with a slight pressure decrease ($\sim 0.2$ GPa corresponding to $\sim 7$ km of crustal thinning). This temperature increase, probably progressive, may have been responsible, for the first time, for the transformation of kyanite into prismatic sillimanite. Then, this transformation was followed by the moderate deformation of newly crystallized sillimanites through dislocation creep and dynamic recrystallization. This heating may also account for the crystallization of Ca-rich osumilite in the G2 and G3 granulites, likely resulting from the reaction $Grt + Feldspar + Qz \rightarrow Os + Opx$, as proposed by Audibert et al. (1995). In our case, osumilite is Ca-rich (up to 4 wt %), and the feldspar implicated in the reaction is probably plagioclase. Approaching peak temperature, anhydrous partial melting may have been triggered. This melting episode may be responsible for melt percolation followed by crystallization of interstitial quartz and feldspars in the QFG matrix and possibly also for the formation of restitic granulites.

– Equilibrium temperatures estimated from feldspars in the QFG matrix are significantly lower (around 750–830 °C) than those recorded by the two previous parageneses. These low temperatures probably correspond to the cooling of the lower crust after the peak temperature of the second stage.

The restitic granulites likely underwent a sequence of events similar to the QFG but with different intensities. Assuming that these rocks were initially quartzo-feldspathic, the first part of their evolution was likely similar to the QFG granulites, especially regarding the transformation of kyanite into sillimanite at the onset of the heating episode. The restitic mineral composition of these rocks, together with their structure, supports that they have undergone a subsequent episode of partial melting, leading to the almost complete consumption and extraction of quartz and feldspars. The resulting lack of quartz and feldspars in the RG may have favored the reaction between sillimanite and garnet. The peculiar microstructure of TAF500 (lobate shape of sillimanites and continuous spinel corona around them, skeletal shape of garnet, and interstitial Opx wrapping garnets) might be explained by an intensification of the reaction between garnet and sillimanite after the consumption of quartz and feldspars.

Two hypotheses can be proposed to explain the formation of the RG. In the first one, the extraction of the quartzo-feldspathic component would have occurred due to the partial melting triggered in the QFG granulites by temperature increase ($\sim 1100$ °C) at the end of the ultrahigh thermal event. The second hypothesis considers that the thermal event responsible for the formation of RG results from the Middle Atlas Plio-Quaternary volcanic activity. In the later case, the RG might represent restitic walls of basaltic dikes emplaced before the entrapment of xenoliths by the eruption of Tafraoute maar, as proposed in the cartoon of Fig. 12. The formation of Sp coronas around sillimanite and of the poikilitic large interstitial crystal of Opx present in TAF500 might be associated with this event, perhaps after the melting of the quartzo-feldspathic phases and the extraction of the resulting melt. The percolation of an $H_2O$- and $CO_2$-rich and $SiO_2$-undersaturated liquid issued from the dikes might have triggered, for the first time, an almost complete in situ dissolution of the Opx from the kelyphitic corona around garnet (Shaw, 1999) associated with a peripheral dissolution of sillimanite (and possibly also of ilmenite rims in contact with the melt). Shortly thereafter, this dissolution may have been followed by crystallization, also in situ, of poikilitic Opx and the formation of spinel coronas around sillimanite.

The presence in the RG, and to a lesser extend in the QFG, of pockets of vesicular and more or less dark brown glass containing minute crystals (Al–Opx, Sp, Il, and TM) points to a final episode of flash melting followed by fast
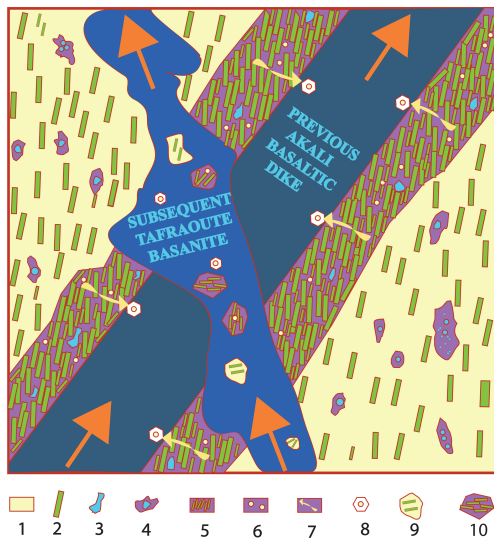
**Figure 12.** Cartoon (not to scale) showing the possible relationships in depth between the different rocks and minerals found as xenolith and megacrysts in the Tafraoute tuffs (1) quartzo-feldspathic granulite, (2) prismatic sillimanite, (3) garnet, (4) kelyphitization corona, (5) restitic granulite, (6) anhedral corundum in restitic rock, (7) melt issued from partial melting of the dike wall, (8) corundum megacryst, (9) quartzo-feldspathic granulite xenolith, and (10) restitic granulite xenolith. The Plio-Quaternary volcanic episode started with the injection of early basaltic dikes that may have been responsible for the partial melting of their walls and formation of refractory granulites (5). Through the reaction between the melt resulting from partial melting (7) of the walls and the basalt of the dikes, corundum megacrysts (8) may have crystallized. Later on, basaltic eruptions such as those of Tafraoute have carried samples of these various materials up to the surface.

cooling. This late flash melting is probably linked to the entrapment and fast transport of xenoliths up to the surface by Tafraoute basanite (650 ka). The equilibrium temperature between 1020 and 1150 °C estimated from the minerals inside the glass agrees with this hypothesis. This temperature is akin to those usually measured for basaltic magma.

## 7.1   The corundum megacrysts

How to integrate the crystallization of idiomorphic corundum megacrysts in the evolution of the Tafraoute granulites remains an open question. As previously indicated, the chemical composition of the studied megacryst combines both magmatic and metamorphic characteristics. Their crystallization was probably initiated inside restitic granulites, as supported by the presence of small and anhedral corundum crystals in some restitic samples and the presence of several metamorphic phases (including sillimanite) as inclusions inside corundum megacrysts. Since corundum was not encountered in the studied quartzo-feldspathic granulites, this mineral likely formed at the same time as the granulites acquired their refractory characters through overheating and

felsic phase melting. But the acquisition of large sizes and automorphy by megacrysts probably requires further free growth in liquid. As proposed above, the restitic granulites might represent walls of alkali basaltic dikes emplaced before the Tafraoute eruption (Fig. 12). The percolation of $SiO_2$-undersaturated and $H_2O$–$CO_2$-rich fluid issued from lava dikes inside the restitic walls might have led to inter-element exchanges and desilication reactions favoring corundum formation within the restites. Subsequently, the restitic walls were disintegrated by ascending magma, and the corundum crystals were released from their rock matrix. The Si- and Al-rich melt resulting from the melting of walls felsic phases might have been simultaneously incorporated into the lava. The incorporation of such a melt into Si-undersaturated alkali magma would favor the corundum growth and acquisition of idiomorphy, a process already suggested by Coenraads et al. (1990) and Giuliani et al. (2009). But, in our case, this scenario is only based on the study of a single megacryst. A study on a larger number of samples will have to be carried out to have a more precise idea of the origin of the Tafraoute corundum megacrysts.

## 7.2   Microstructures and textures

Both types of granulites display a foliation essentially marked by the orientation of sillimanite and, in the QFG, by quartz and feldspars layers. The large prismatic crystals of sillimanite display uncommon evidence of intracrystalline deformation, with subgrain boundaries that are normal to [001], fan-like crystals, and recrystallized new grains (Fig. 4). This substantiates a moderate crystal plastic deformation of these high-strength prismatic sillimanite after their crystallization. The microstructure formed during this episode was subsequently modified by the UHT partial melting. The crystallographic-preferred orientation of sillimanite, although rather weak, is well defined and displays a concentration of [001] parallel to the foliation, which marks the lineation (Fig. 10). Together with subgrain boundaries dominantly orthogonal to [001], this preferred orientation supports that [001] was the dominant slip direction of dislocations during deformation.

Garnet crystals display scarce evidence of solid-state deformation, with the weak bending of the crystal lattice, elongated shape, and fractures. In both granulite types, garnets are partially to almost totally destabilized (Figs. 3, 5, and S2), and the products of its breakdown do not display evidence of solid-state deformation or any reliable CPO (Figs. 10 and S8–S9). This strongly supports the idea that these rocks were not deformed after the garnet breakdown and, thus, that the latter occurred after the deformation of sillimanite.

Quartz in the felsic layers does not display evidence of internal solid-state deformation, but it sometimes displays evidence of annealing and grain boundary migration (straight boundaries and 120° triple junctions). Similarly, small grains of K-feldspar frequently show evidence of annealing and

grain boundary migration. However, in sample G2 (Fig. 3), perthitic K-feldspars porphyroclasts displaying a faint undulose extinction are surrounded by small KF grains following their irregular boundary. These aggregates of small KF grains also involve tiny plagioclase grains. This microstructure is suggestive of dynamic recrystallization leading to the crystallization of albite-rich Plg from perthites. In addition, in several samples, such as G4, most quartz and KF crystals have an interstitial habitus and are locally clustered in elongated aggregates oblique to the foliation. These observations are pointing to a crystallization from a percolating melt after deformation has stopped. Plagioclase displays microstructures similar to quartz and K-feldspars, although there is less evidence of late crystallization from the percolating melt from which quartz and K-feldspar interstitial grains crystallized.

In samples G2 and G3, quartz displays a weak [0001]-axial CPO poorly correlated with the sillimanite CPO. In both cases, the maximum concentration of [0001] is in the foliation plane but is variably oblique (30–45°) relative to the sillimanite [001] axis. Two processes may account for this weak CPO: (1) preservation of some quartz crystals inherited from the initial paragenesis (they have undergone the same solid-state deformation as sillimanites and escaped partial melting) and (2) oriented crystallization from a melt under a moderate stress oriented differently to the one responsible for the deformation of sillimanite. Sample G4 does not display any reliable preferred orientation of quartz, which is in agreement with the interstitial habitus of this phase and, thus, with crystallization from a percolating melt under static conditions.

In all studied samples, KF and Plg do not display any reliable preferred orientation. This is in good agreement with a post-kinematic crystallization of most feldspars from a melt. Nevertheless, the presence of inherited porphyroclasts in some samples supports that this melt would result from late partial melting of primary quartzo-feldspathic layers.

Altogether, these observations support that the evolution of the Tafraoute granulites occurred during a progressive temperature increase (Fig. 11) followed by cooling. In the first time, the temperature increase coeval with strain were responsible for the transformation of kyanite in prismatic sillimanite, as suggested above, and for its deformation. This deformation likely ended before the high temperature breakdown of garnet as supported by the lack of deformation of destabilization products. In this scheme, the crystallization of interstitial quartz and feldspars grains observed in the QFG likely resulted from the subsequent crystallization of a percolating melt due to the partial melting of original quartzo-feldspathic layers. Indeed, considering the peak-temperatures recorded by these samples, cooling of the lower crust was probably slow and, thus, the crystallization of melts was delayed.

The microstructural and mineralogical peculiarities of the restitic granulites suggest that they reacted more intensely to a thermal event (either associated with the paragenesis (P II)

or to the emplacement of basaltic dikes in the lower crust). Despite this evolution, the internal deformation and CPO of sillimanites have been preserved.

## 7.3 Comparison of the Tafraoute and Beni Bousera lower-crust evolution (Fig. 11)

The primary paragenesis recorded by the Tafraoute QFG was probably similar to the Beni Bousera Hercynian granulite one (El Maz and Guiraud, 2001), suggesting that it is also Hercynian in age. The initial likeness of the Beni Bousera and Tafraoute lower crust is strengthened by the similarity of the shallower lithospheric mantle from the Rif range to the Middle Atlas before the Alpine orogenic event (Pezzali et al., 2015). However, the Tafraoute QFG differ from Beni Bousera ones by the presence of deformed large prismatic sillimanite, Opx + Os in Grt coronas, by the lack of biotite and secondary cordierite, and by evidence of subsequent heating to ultrahigh temperature. These differences support the idea that the Hercynian QFG from Tafraoute and Beni Bousera, initially almost similar, have undergone drastically different subsequent evolutions (Fig. 11). The post-Hercynian evolution of Beni Bousera granulites is characterized by an almost adiabatic decompression of ∼ 0.8 GPa due to their exhumation during the alpine orogeny (El Maz and Guiraud, 2001; Álvarez-Valero et al., 2014; El Bakili et al., 2020; Rossetti et al., 2020; Fig. 11). Contrastingly, the Tafraoute granulites were not exhumed and recorded a temperature increase (∼ 200 °C) of the lower crust, possibly associated with a slight $P$ decrease (≤0.3 GPa).

Altogether, these results suggest that the lower crust under north Morocco, at least between the Rif and the Middle Atlas, underwent rather homogeneous metamorphic conditions during the Hercynian orogeny, as already suggested by Rossetti et al. (2020). This favors the hypothesis that the temperature increase (∼ 200 °C) suffered by the Tafraoute lower crust was related to a post-Hercynian event, which was likely pre-alpine or alpine.

## 7.4 A possible scenario for the evolution of the Tafraoute lower crust

At the location of the future Middle Atlas belt, the Alpine deformation was preceded by a Triassic–Jurassic episode of rifting linked to the central Atlantic opening (e.g., Michard et al., 2008, and references therein). In the tabular Middle Atlas, where the Tafraoute maar is located, the alpine deformation was limited to local fault reactivation (Gomez et al., 1996; Zeyen et al., 2005; Frizon de Lamotte et al., 2008; Saura et al., 2014). This favors the hypothesis that the post-Hercynian tectono-metamorphic evolution of the Tafraoute lower crust was rather related to the Mesozoic pre-alpine rifting.

In this hypothesis, the Tafraoute Hercynian crust (around 40 km thick and with temperatures in the lower crust likely 850–880 °C at the end of the Hercynian orogeny) may have

been slightly thinned by $\sim 7$ km, simultaneously with an increase in temperature of $\sim 200\,°C$ compared to the temperature recorded by the granulite garnet inclusions. This high temperature increase for such a limited thinning may be due to two possibly complementary processes, namely (1) thinning of the crust associated with mantle upwelling and (2) emplacement of gabbro bodies in, or just below, the lower crust. This second process is supported by the presence of many undeformed subalkaline gabbro xenoliths in the Tafraoute tuffs, which are alike to Mesozoic gabbro intrusions reported in many places within the Atlas belt (e.g., Hailwood and Mitchell, 1971; Smith and Pozzobon, 1979; Westphal et al., 1979; Calvin et al., 2017, and references therein). This scenario is consistent with the mineralogical, microstructural, and CPO data and the continuous evolution presented above.

# 8 Conclusion

The tuffs of the Quaternary Tafraoute maar (Tabular Middle Atlas, north Morocco) contain two types of lower-crustal sillimanite- and garnet-rich metapelitic granulites: layered quartzo-feldspathic ones and restitic ones. Combining the new data obtained from these granulites with those acquired from mantle xenoliths sampled in the same maar and with available geophysical data on the Middle Atlas, we propose an evolution of the lower crust beneath the Middle Atlas. This evolution would involve two tectono-metamorphic events followed by an ultimate flash heating and fast decompression related to the maar eruption.

- During the first event, the lower crust acquired its foliation and yield equilibrium $P$ and $T$ conditions of $1.1 \pm 0.1$ GPa and 850–880 °C, which are similar to the ones of lower-crustal granulites from the Rif. Under these conditions, the Al silicate present in the rocks was likely kyanite, and the primary paragenesis also comprised garnet, rutile, plagioclase, perthitic K-feldspar, quartz, graphite, and ilmenite. As supported by the absence of biotite, these rocks probably underwent fluid-absent partial melting. This event may correspond to the Hercynian orogeny as this was established in the Rif belt.

- The second tectono-metamorphic event is characterized by a progressive reheating up to ultrahigh temperatures ($1050 \pm 50$ °C) under slightly lower-pressure conditions ($0.9 \pm 0.1$ GPa). This would have first triggered the transformation of kyanite into sillimanite. After its crystallization, sillimanite experienced a moderate crystal plastic deformation that likely also affected quartz and feldspars. This deformation was followed by stress relaxation under persisting ultrahigh temperature metamorphic conditions that initiated garnet breakdown through the reaction $Grt + Sil \rightarrow Al–Opx + Sp$

($\pm Plg \pm Qz$). Reaching peak temperatures, anhydrous partial melting of felsic layers occurred in quartzo-feldspathic granulites, and the resulting melt spread through the rocks. Then, the temperature progressively dropped to $\sim 800$ °C, leading to static crystallization of deformation-free interstitial quartz and feldspars from the melt. This second tectono-metamorphic event probably results from Triassic–Jurassic rifting, possibly coeval with underplating of gabbroic magma. In this hypothesis, considering the lack of deformation subsequent to the crystallization of quartz and feldspars from the melt produced by the second tectono-metamorphic event, the lower crust of the tabular Middle Atlas was not significantly affected by the alpine, Cretaceous–Eocene, compression. This hypothesis agrees with the preservation of geochemical characteristics typical of the extension in the upper mantle (El Messbahi et al., 2015).

- The following two hypotheses may explain the formation of the restitic granulites: (1) they might be due to the UHT melting event through almost total consumption of quartz and feldspars and extraction of the resulting melt, and (2) they might represent the walls of basaltic dikes emplaced during the long-lasting (Miocene to Quaternary) volcanic activity in the Middle Atlas. The studied RG might represent pieces of these walls extracted as xenoliths.

- The last event, recorded by all studied granulites, results from their entrapment in the host basanitic lava and their very fast transfer to the surface by the Tafraoute maar eruption that occurred in 650 ka. During this event, the sampled granulites have been heated up to 1150 °C, producing vesicular glass that partially crystallized during the fast decompression and cooling.

## References

Albarède, F.: How deep do common basaltic magmas form and differentiate?, J. Geophys. Res., 97, 10997–11009, https://doi.org/10.1029/91JB02927, 1992.

Álvarez-Valero, A. M., Jagoutz, O., Stanley, J., Manthei, C., El Maz, A., Moukadiri, A., and Piasecki, A.: Crustal attenuation as a tracer for the emplacement of the Beni Bousera ultramafic massif (Betico-Rifean belt), Geol. Soc. Am. Bull., 126, 1614–1624, https://doi.org/10.1130/B31040.1, 2014.

Aranovich, l. Y. and Berman, R. G.: A new garnet-orthopyroxene thermometer based on reversed $Al_2O_3$ solubility in FeO–$Al_2O_3$–$SiO_2$ orthopyroxene, Am. Mineral., 82, 345–353, https://doi.org/10.2138/am-1997-3-413, 1997.

Audibert, N., Hensen, B. J., and Bertrand, P.: Experimental study of phase relationships involving osumilite in the system $K_2O$–FeO–MgO–$Al_2O_3$–$SiO_2$–$H_2O$ at high pressure and high temperature, J. Metamorph. Geol., 13, 331–344, https://doi.org/10.1111/j.1525-1314.1995.tb00223.x, 1995.

Bachmann, F., Hielscher, R., and Schaeben, H.: Texture Analysis with MTEX – Free and Open Source Software Toolbox, Solid State Phenomen., 160, 63–68, https://doi.org/10.4028/www.scientific.net/SSP.160.63, 2010.

Bachmann, F., Hielscher, R., and Schaeben, H.: Grain detection from 2d and 3d EBSD data-Specification of the MTEX algorithm, Ultramicroscopy, 111, 1720–1733, https://doi.org/10.1016/j.ultramic.2011.08.002, 2011.

Baldwin, J. A., Powell, R., Brown, M., Moraes, R., and Fuck, R. A.: Modelling of mineral equilibria in ultrahigh-temperature metamorphic rocks from the Anapolis–Itauçu Complex, central Brazil, J. Metamorph. Geol., 23, 511–531, https://doi.org/10.1111/j.1525-1314.2005.00591.x, 2005.

Baptiste, V., Tommasi, A., Vauchez, A., Demouchy, S., and Rudnick, R. L.: Deformation, hydration, and anisotropy of the lithospheric mantle in an active rift: Constraints from mantle xenoliths from the North Tanzanian Divergence of the East African Rift, Tectonophysics, 639, 34–55, https://doi.org/10.1016/j.tecto.2014.11.011, 2015.

Barbosa, J., Nicollet, C., and Leite, C.: Hercynite-Quartz-Bearing Granulites from Brejoes Dome Area, Jequié Block, Bahia, Brazil: Influence of Charnockite Intrusion on Granulite Facies Metamorphism, Lithos, 92, 537–556, https://doi.org/10.1016/j.lithos.2006.03.064, 2006.

Beattie, P.: Olivine-melt and orthopyroxene-melt equilibria, Contrib. Mineral. Petr., 115, 103–111, https://doi.org/10.1007/BF00712982, 1993.

Benisek, A., Dachs, E., and Kroll, H.: A ternary feldspar mixing model based on calorimetric data: development and application, Contrib. Mineral. Petr., 160, 327–337, https://doi.org/10.1007/s00410-009-0480-8, 2010.

Bhattacharia, S. and Kar, R.: High temperature dehydration melting and decompressive P–T path in a granulite complex from the Eastern Ghats, India, Contrib. Mineral. Petr., 143, 175–191, https://doi.org/10.1007/s00410-001-0341-6, 1996.

Bohlen, S. R.: On the formation of granulites, J. Metamorph. Geol., 96, 223–229, https://doi.org/10.1111/j.1525-1314.1991.tb00518.x, 1991.

Bohlen, S. R., Wall, V. J., and Boettcher, A. L.: Experimental investigations and geological applications of equilibria in the system: FeO–$TiO_2$–$Al_2O_3$–$H_2O$, Am. Mineral., 68, 1049–1058, 1983.

Caddick, M. J. and Thompson, A. B.: Quantifying the tectonometamorphic evolution of pelitic rocks from a wide range of tectonic settings: Mineral compositions in equilibrium, Contrib. Mineral. Petr., 156, 177–195, https://doi.org/10.1007/s00410-008-0280-6, 2008.

Calvín, P., Ruiz-Martínez, V. C., Villalaín, J. J., Casas-Sainz, A. M., and Moussaid, B.: Emplacement and deformation of Mesozoic gabbros of the High Atlas (Morocco): Paleomagnetism and magnetic fabrics, Tectonics, 36, 3012–3037, https://doi.org/10.1002/2017TC004578, 2017.

Charlier, B., Skar, O., Korneliussen, A., Duchesne, J. C., and Auwera, J. V.: Ilmenite composition in the Tellnes Fe–Ti deposit, SW Norway: fractional crystallization, postcumulus evolution and ilmenite–zircon relation, Contrib. Mineral. Petr., 154, 119–134, 2007.

Chopin, F., Corsini, M., Schulmann, K., El Houicha, M., Ghienne, J. F., and Edel, J. B.: Tectonic evolution of the Rehamna metamorphic dome (Morocco) in the context of the Alleghanian-Variscan orogeny, Tectonics, 33, 1154–1177, https://doi.org/10.1002/2014TC003539, 2014.

Coenraads, R. R., Sutherland, F. L., and Kinny P. D.: The origin of sapphires: U–Pb dating of zircon inclusions sheds new light, Mineral. Mag., 54, 113–122, https://doi.org/10.1180/minmag.1990.054.374.13, 1990.

Das, K., Dasgupta, S., and Miura, H.: Stability of osumilite coexisting with spinel solid solution in metapelitic granulites at high oxygen fugacity, Am. Mineral., 86, 1423–1434, https://doi.org/10.2138/am-2001-11-1211, 2001.

Diener, J. F. A. and Powell, R.: Influence of ferric iron on the stability of mineral assemblages, J. Metamorph. Geol., 28, 599–613, https://doi.org/10.1111/j.1525-1314.2010.00880.x, 2010.

Droop, G.: A general equation for estimating $Fe^{3+}$ concentrations in ferromagnesian silicates and oxides from microprobe analyses, using stoichiometric criteria, Mineral. Mag., 51, 431–435, https://doi.org/10.1180/minmag.1987.051.361.10, 1987.

El Azzouzi, M., Maury, R. C., Bellon, H., Youbi, N., Cotton, J., and Kharbouch, F.: Petrology and K-Ar chronology of the Neogene-Quaternary Middle Atlas basaltic province, Morocco, B. Soc. Géol. Fr., 181, 243–257, https://doi.org/10.2113/gssgfbull.181.3.243, 2010.

El Bakili, A., Corsini, M., Chalouan, A., Münch, P., Romagny, A., Lardeaux, J. M., and Azdimousa, A.: Neogene polyphase deformation related to the Alboran Basin evolution: new insights for the Beni Bousera massif (Internal Rif, Morocco), B. Soc. Géol. Fr., 191, 1–18, https://doi.org/10.1051/bsgf/2020008, 2020.

El Maz, A. and Guiraud, M.: Paragenèse à faible variance dans les métapélites de la série de Filali (Rif interne marocain): description, interprétation et conséquence géodynamique, B. Soc. Géol. Fr., 172, 469–485, https://doi.org/10.2113/172.4.469, 2001.

El Messbahi, H., Bodinier, J. L., Vauchez, A., Dautria, J. M., Ouali, H., and Garrido, C. J.: Short wavelength lateral variability of lithospheric mantle beneath the Middle Atlas (Morocco) as recorded by mantle xenoliths, Tectonophysics, 650, 34–52, https://doi.org/10.1016/j.tecto.2014.11.020, 2015.

El Messbahi, H., Dautria, J. M., Jourde, H., Munch, P., Alard, O., Bodinier, J. L., and Ouali, H.: Eruption dynamics of pleistocene maars and tuff rings from the Azrou Timahdite district (Middle Atlas, northern Morocco) and its relevance to environmental changes and ground water table characteristics, J. Afr. Earth Sci., 167, 1–20, https://doi.org/10.1016/j.jafrearsci.2020.103845, 2020.

Essene, E. J.: The current status of thermobarometry in metamorphic rocks, Geol. Soc. London Spec. Publ., 43, 1–44, https://doi.org/10.1144/GSL.SP.1989.043.01.02, 1989.

Fiechtner, L., Friedrichsen, H., and Hammerschmid, K.: Geochemistry and geochronology of Early Mesozoic tholeiites, Geol. Rundsch., 81/1, 45–62, https://doi.org/10.1007/BF01764538, 1992.

Frizon de Lamotte, D., Saint Bezar, B., Bracène, E., and Mercier, E.: The two main steps of the Atlas building and geodynamics of the western Mediterranean, Tectonics, 19, 40–761, https://doi.org/10.1029/2000TC900003, 2000.

Frizon de Lamotte, D., Zizi, M., Missenard, Y., Hafid, M., Elazzouzi, M., Charrière, A., Maury, R. C., Taki, Z., Benammi, M., and Michard, A.: The Atlas system, in: Continental Evolution: The Geology of Morocco, edited by: Michard, A., Saddiqi, O., Chalouan, A., and Frizon de Lamotte, D., Structure, Stratigraphy, and Tectonics of the Africa-Atlantic-Mediterranean Triple Junction, Springer-Verlag, 133–202, https://doi.org/10.1007/978-3-540-77076-3_4, 2008.

Giuliani, G., Fallick, A., Ohnenstetter, D., and Pegere, G.: Oxygen isotopes composition of sapphires from the French Massif Central: implications for the origin of gem corundum in basaltic fields, Miner. Deposita, 44, 221–231, https://doi.org/10.1007/s00126-008-0214-2, 2009.

Gomez, F., Barazang, M., and Bensaid, M.: Active tectonism in the intracontinental Middle Atlas Mountains of Morocco: synchronous crustal shortening and extension, J. Geol. Soc. London, 153, 389–402, https://doi.org/10.1144/gsjgs.153.3.0389, 1996.

Guiraud, M., Kienast, J. R., and Ouzegane, K.: Corundumquartz-bearing assemblage in the Ihouhaouene area (In Ouzzal, Algeria), J. Metamorph. Geol., 14, 755–761, https://doi.org/10.1111/j.1525-1314.1996.00046.x, 1996a.

Guiraud, M., Kienast, J. R., and Rahmani, A.: Petrological study of high-temperature granulites from In Ouzzal, Algeria: some implications on the phase relationships in the FMASTOCr system, Eur. J. Mineral., 8, 1375–1390, https://doi.org/10.1127/ejm/8/6/1375, 1996b.

Guo, J., O'Reilly, S. Y., and Griffin, W. L.: Corundum from basaltic terrains: a mineral inclusion approach to the enigma, Contrib. Mineral. Petr., 122, 368–386, https://doi.org/10.1007/s004100050134, 1996.

Hailwood, E. A. and Mitchell, J. C.: Paleomagmatic and radiometric dating results from Jurassic in South Morroco, Geophys. J. Roy. Astr. S., 24, 351–364, https://doi.org/10.1111/j.1365-246X.1971.tb02183.x, 1971.

Harley, S. L.: An experimental study of the partitioning of Fe and Mg between garnet and orthopyroxene, Contrib. Mineral. Petr., 86, 359–373, https://doi.org/10.1007/BF01187140, 1984.

Harley, S. L.: The origins of granulites: a metamorphic perspective, Geol. Mag., 126, 215–247, https://doi.org/10.1017/S0016756800022330, 1989.

Harley, S. L.: On the occurrence and characterization of ultrahigh-temperature crustal metamorphism, Geol. Soc. London Spec. Publ., 138, 81–107, https://doi.org/10.1144/GSL.SP.1996.138.01.06, 1998.

Harley, S. L.: Refining the $P–T$ records of UHT crustal metamorphism, J. Metamorph. Geol., 26, 125–154, https://doi.org/10.1111/j.1525-1314.2008.00765.x, 2008.

Harley, S. L. and Green, D. H.: Garnet-orthopyroxene barometry for granulites and peridotites, Nature, 300, 23–30, https://doi.org/10.1038/300697a0, 1982.

Hensen, B. J. and Green, D. H.: Experimental study of the stability of cordierite and garnet in pelitic compositions at high pressures and temperatures: III. Synthesis of experimental data and geological applications, Contrib. Mineral. Petr., 38, 151–166, https://doi.org/10.1007/bf00373879, 1973.

Hielscher, R.: MTEX, Version 1.0, MATLAB and C subroutine library, http://code.google.com/p/mtex/ (last access: 18 December 2024), 2008.

Hielscher, R. and Schaeben, H.: A novel pole figure inversion method: specification of the MTEX algorithm, J. Appl. Crystallogr., 41, 1024–1037, https://doi.org/10.1107/S0021889808030112, 2008.

Hoepffner, C., Soulaimani, A., and Piqué, A.: The Moroccan hercynides, J. Afr. Earth Sci., 43, 144–165, https://doi.org/10.1016/j.jafrearsci.2005.09.002, 2005.

Holdaway, M. J. and Mukhopadhyay, B.: A reevaluation of the stability relations of andalusite: thermochemical data and phase diagram for the aluminum silicates, Am. Mineral., 78, 298–315, 1993.

Holland, T. J. B. and Powell, R.: An internally consistent dataset for phases of petrological interest, J. Metamorph. Geol., 16, 309–343, https://doi.org/10.1111/j.1525-1314.1998.00140.x, 1998.

Holness, M. B. and Sawyer, E.: On the Pseudomorphing of Melt-filled Pores During the Crystallization of Migmatites, J. Petrol., 49, 1343–1363, https://doi.org/10.1093/petrology/egn028, 2008.

Kelsey, D. E. and Hand, M.: On ultrahigh temperature crustal metamorphism: Phase equilibria, trace element thermometry, bulk composition, heat sources, timescales and tectonic settings, Geosci. Front., 6, 311–356, https://doi.org/10.1016/j.gsf.2014.09.006, 2015.

Kornprobst, J.: Le massif ultrabasique des Beni Bouchera (Rif Interne, Maroc): Etude des péridotites de haute température et de haute pression, et des pyroxénolites, à grenat ou sans grenat, qui leur sont associées, Contrib. Mineral. Petr., 23, 283–322, https://doi.org/10.1007/bf00371425, 1969.

Koziol, A. M. and Newton, R. C.: Grossular activity-composition relationships in ternary garnets determined by reversed displaced-equilibrium experiments, Contrib. Mineral. Petr., 103, 423–433, https://doi.org/10.1007/BF01041750, 1989.

Lal, R. K., Ackermand, D., Raith, M., Raase, P., and Seifert, F.: Sapphirine-bearing assemblages from Kiranur, Southern India: a study of chemographic relationships in the $Na_2O–FeO–MgO–Al_2O_3–SiO_2–H_2O$ system, N. Jb. Mineral Abh., 150, 121–150, 1984.

Lepage, L. D.: ILMAT: An excel worksheet for ilmenite–magnetite geothermometry and geobarometry, Comput. Geosci., 29, 673–678, https://doi.org/10.1016/S0098-3004(03)00042-6, 2003.

Leyreloup, A.: Les enclaves catazonales remontées par les éruptions néogènes de France: nature de la croûte inférieure, Contrib. Mineral. Petr., 46, 17–27, https://doi.org/10.1007/BF00377990, 1974.

Lindsley, D. H. and Spencer, K. J.: Fe-Ti oxide geothermometry: Reducing analyses of coexisting Ti-magnetite (Mt) and ilmenite (Ilm) abstract AGU 1982 Spring Meeting, EOS T. Am. Geophys. Un., 63, 471, 1982.

Mainprice, D., Bachmann, F., Hielscher, R., and Schaeben, H.: Descriptive tools for the analysis of texture projects with large datasets using MTEX: strength, symmetry and components, Geol. Soc. London Spec. Publ., 409, 251–271, https://doi.org/10.1144/SP409.8, 2014.

Martignole, J. and Martelat, J. E.: Regional-scale Grenvillianage UHT metamorphism in the Mollendo-Camana Block (basement of the Peruvian Andes), J. Metamorph. Geol., 1, 99–120, https://doi.org/10.1046/j.1525-1314.2003.00417.x, 2003.

Mattauer, M., Tapponnier, P., and Proust, F.: Sur les mécanismes de formation des chaînes intracontinentales: l'exemple des chaînes atlasiques du Maroc, B. Geol. Soc. Fr., 77, 521–526, https://doi.org/10.2113/gssgfbull.S7-XIX.3.521,1977.

Melchiorre, M., Alvarez-Valero, A. M., Fernandez, J. V. M., Belousova, E. A., El Maz, A., and Moukadiri, A.: In situ U–Pb zircon geochronology on metapelitic granulites of Beni Bousera (Betic-Rif system, N Morocco), Geol. Soc. Am. Spec. Pap., 526, 151–171, https://doi.org/10.1130/2017.2526(08), 2017.

Michard, A., Saddiqi, O., Chalouan, A., and Frizon de Lamotte, D.: The Variscan belt in Continental evolution: the geology of Morocco: structure, stratigraphy and tectonics of the Africa-Atlantic-Mediterranean triple junction, Lecture notes in Earth Sciences, Springer-Verlag, https://doi.org/10.1007/978-3-540-77076-3, 2008.

Miyashiro, A.: Osumilite, a new silicate mineral, and its crystal structure, Am. Mineral., 41, 104–116, 1956.

Montel, J. M., Kornprobst, J., and Vielzeuf D.: Preservation of old U–Th–Pb ages in shielded monazites: exemple from the Beni Bousera hercynian kinzigites (Morocco), J. Metamorph. Geol., 18, 335–342, https://doi.org/10.1046/j.1525-1314.2000.00261.x, 2000.

Moukadiri, A. and Boulouton, J.: Petrology of granulitic xenoliths in Neogene volcanic rocks of the Middle Atlas: implications for the lower crust of central Morocco, CR Acad. Sci. Paris, 327, 731–734, https://doi.org/10.1016/S1251-8050(99)80043-3, 1998.

Nair, R. and Chacko, T.: Fluid-absent Melting of High-grade Semipelites: $P–T$ Constraints on Orthopyroxene Formation and Implications for Granulite Genesis, J. Petrol., 43, 2121–2142, https://doi.org/10.1093/petrology/43.11.2121, 2002.

Nekvasil, H. and Burnham, C. W.: The calculated individual effects of pressure and water content on phase equilibiria in the granite system, in: Magmatic processes: physicochemical principles, edited by: Mysen, B. O., Geol. Soc. Spec. Publ., 1, 433–445, ISBN 0-941809-00-5, 1987.

Newton, R. C. and Haselton, H. T.: Thermodynamics of the garnet–plagioclase–$Al_2SiO_5$–quartz geobarometer, in: Thermodynamics of minerals and Melts, edited by: Newton, R. C., Navrotsky, A., and Wood, B. J., Springer-Verlag, New York, 129–145, https://doi.org/10.1007/978-1-4612-5871-1_7, 1981.

Newton, R. C. and Perkins III, D.: Thermodynamic calibration of geobarometers based on the assemblages garnet-plagioclase-orthopyroxene (clinopyroxène)-quartz, Am. Mineral., 67, 203–222, 1982.

Nickel, K. G. and Green, D. H.: Emperical geothermobarometry for garnet peridotites and implications for the nature of lithosphere kimberlites and diamonds, Earth Planet. Sc. Lett., 73, 158–170, https://doi.org/10.1016/0012-821X(85)90043-3, 1985.

Ouzegane, K., Guiraud, M., and Kienast, J. R.: Prograde and Retrograde Evolution in High-temperature Corundum Granulites (FMAS and KFMASH Systems) from In Ouz-

zal Terrane (NW Hoggar, Algeria), J. Petrol., 44, 517–545, https://doi.org/10.1093/petrology/44.3.517, 2003a.

Ouzegane, K., Kienast, J. R., Bendaoud, A., and Drareni, A.: A review of Archaean and Paleoproterozoic evolution of the In Ouzzal granulitic terrane (Western Hoggar, Algerian), J. Afr. Earth Sci., 37, 207–227, https://doi.org/10.1016/j.jafrearsci.2003.05.002, 2003b.

Peucat, J. J., Ruffault, P., Fritsch, E., Bouhnik-Le Coz, M., Simonet, C., and Lasnier, B.: Ga/Mg ratio as a new geochemical tool to differentiate magmatic from metamorphic blue sapphires, Lithos, 98, 261–274, https://doi.org/10.1016/j.lithos.2007.05.001, 2007.

Pezzali, I., France, L., Chazot, G., and Vannucci, R.: Analogues of exhumed pyroxenite layers in the Alboran domain sampled as xenoliths by Middle Atlas Cenozoic volcanism, Lithos, 230, 184–188, https://doi.org/10.1016/j.lithos.2015.02.024, 2015.

Piazolo, S. and Jaconelli, P.: Sillimanite deformation mechanisms within a Grt-Sil-Bt gneiss: effect of pre-deformation grain orientations and characteristics on mechanism, slip-system activation and rheology, Geol. Soc. London Special Publications, 394, 189–213, https://doi.org/10.1144/SP394.10, 2013.

Piqué, A. and Michard, A.: Moroccan Hercynides: a synopsis. The Paleozoic sedimentary and tectonic evolution at the northern margin of West Africa, Am. J. Sci., 289, 286–330, https://doi.org/10.2475/ajs.289.3.286, 1989.

Price, J. G.: Ideal site mixing in solid solutions, with an application to two-feldapar geothermometry, Am. Mineral., 70, 696–701, 1985.

Putirka, K.: Thermometers and Barometers for Volcanic Systems, in: Minerals, Inclusions and Volcanic Processes, edited by: Putirka, K.and Tepley, F., Rev. Mineral. Geochem., 69, 61–120, https://doi.org/10.2138/rmg.2008.69.3, 2008.

Raith, M., Karmakar, S., and Brown, M.: Ultrahigh-temperature metamorphism and multi-stage decompressional evolution of sapphirine granulites from the Palni Hill Ranges, Southern India, J. Metamorph. Geol., 15, 379–399, https://doi.org/10.1111/j.1525-1314.1997.00027.x, 1997.

Rossetti, F., Lucci, F., Theye, T., Bouybaouène, M., Gerdes, A., Opitz, J., Dini, A., and Lipp, C.: Hercynian anatexis in the envelope of the Beni Bousera peridotites (Alboran Domain, Morocco): Implications for the tectono-metamorphic evolution of the deep crustal roots of the Mediterranean region, Gondwana Res., 83, 157–182, 2020.

Sato, K., Miyamoto, T., and Kawasaki, T.: $Fe^{2+}$–Mg partitioning experiemts between orthopyroxene and spinel using ultrahigh-temperture granulite from the Napier complex, Est Antartica, Geol. Soc. Spec. Publ., 308, 431–447, https://doi.org/10.1144/SP308.22, 2008.

Saura, E., Vergés, J., Martin-Martin, J. D., Messager, G., Moragas, M., Razin, P., Grélaud, C., Joussiaume, R., Malaval, M., Homke, S., and Hunt, D.: Syn- to post-rift diapirism and minibasins of the Central High Atlas (Morocco): the changing face of a mountain belt, J. Geol. Soc. London, 171, 97–105, https://doi.org/10.1144/SP308.22, 2014.

Schumacher, J. C.: Empirical ferric iron corrections: necessity, assumptions, and effect on selected geothermobarometers, Mineral. Mag., 55, 3–18, https://doi.org/10.1180/minmag.1991.055.378.02, 1991.

Shaw, C. S. J.: Dissolution of orthopyroxene in basanitic magma between 0.4 and 2 GPa: further implications for the origin of Si-rich

alkaline glass inclusions in mantle xenoliths, Contrib. Mineral. Petr., 135, 114–132, 1999.

Smith, R. L. and Pozzobon, J. C.: The Imiter gabbroic complex, High Atlas Mountains, Morocco, J. Geol., 87, 317–324, https://doi.org/10.1086/628420, 1979.

Spencer, K. J. and Lindsley, D. H.: A solution model for coexisting iron-titanium oxides, Am. Mineral., 66, 1189–1201, 1981.

Sudholz, Z. J., Green, D. H., Yaxley, G. M., and Jaques, A. L.: Mantle geothermometry: experimental evaluation and recalibration of Fe–Mg geothermometers for garnet-clinopyroxene and garnet-orthopyroxene in peridotite, pyroxenite and eclogite systems, Contrib. Mineral. Petr., 177, 77, https://doi.org/10.1007/s00410-022-01944-3, 2022.

Sutherland, F. L., Hoskin, P. W. O., Fanning, C. M., and Coenraads, R. R.: Models of corundum origin from alkali basaltic terrains: a reappraisal, Contrib. Mineral. Petr., 133, 356–372, https://doi.org/10.1007/s004100050458, 1998.

Tong, L. and Wilson, C. J. L.: Tectonothermal evolution of the ultrahigh temperature metapelites in the Rauer Group, east Antarctica, Precambrian Res., 149, 1–20, https://doi.org/10.1016/j.precamres.2006.04.004, 2006.

Uher, P., Guliani, G., Szakáll, S., Fallick, A., Strunga, V., Vaculovič, T., Ozdín, D., and Gregáňová, M.: Sapphires related to alkali basalts from Cerová Highlands, Western Carpathians (southern Slovakia): composition and origin, Geol. Carpath., 63, 71–82, 2012.

Vielzeuf, D. and Holloway, J. R.: Experimental determination of the fluid-absent melting reactions in the pelitic system, Contrib. Mineral. Petr., 98, 257–276, https://doi.org/10.1007/BF00375178, 1988.

Vielzeuf, D., Clemens, J. D., Pin, C., and Moinet, E.: Granites, Granulites, and Crustal Differentiation, in: Granulites and Crustal Evolution, edited by: Vielzeuf, D. and Vidal, P., NATO ASI Series, vol. 311, Springer, Dordrecht, https://doi.org/10.1007/978-94-009-2055-2_5, 1990.

Wen, S. and Nekvasil, H.: SOLVCALC: An interactive graphics program package for calculating the ternary feldspar solvus and for two-feldspar geothermometry, Comput. Geosci., 20, 1025–1040, https://doi.org/10.1016/0098-3004(94)90039-6, 1994.

Westphal, M., R., Montigny, R., Thuizat, R., Bardon, C., Bossert, A. R., and Hamze, R.: Paleomagnetisme et datation du volcanisme permien, triasique et crétacé du Maroc, Can. J. Earth Sci., 16, 2150–2164, https://doi.org/10.1139/e79-202, 1979.

Wheller, C. J. and Powell, R.: A new thermodynamic model for sapphirine: calculated phase equilibria in $K2O–FeO–MgO–Al_2O_3$–$SiO_2–H_2O–TiO_2–Fe_2O_3$, J. Metamorph. Geol., 32, 287–299, https://doi.org/10.1111/jmg.12067, 2014.

Yardley, B. W. D.: An empirical study of diffusion in garnet, Am. Mineral., 62, 793–800, 1977.

Yavuz, F. and Yavuz, E. V.: A Windows Program for Feldspar Group Thermometers and Hygrometers, Period di Mineral., 91, 63–87, https://doi.org/10.13133/2239-1002/17666, 2022.

Zeyen, H., Ayarza, P., Fernàndez, M., and Rimi, A.: Lithospheric structure under the western African-European plate boundary: A transect across the Atlas Mountains and the Gulf of Cadiz, Tectonics, 24, TC2001, https://doi.org/10.1029/2004TC001639, 2005.